J. Fluid Mech. (2005), *vol.* 528, *pp.* 87–118.
doi:10.1017/S0022112004003283 Printed in the United Kingdom

Lagrangian measurement of vorticity dynamics in turbulent flow

By BEAT LÜTHI[1], ARKADY TSINOBER[2] AND WOLFGANG KINZELBACH[1]

[1]Institut für Hydromechanik und Wasserwirtschaft, ETH Hönggerberg, 8093 Zürich, Switzerland

[2]Faculty of Engineering, Tel Aviv University, 69974, Tel Aviv, Israel

(Received 25 April 2003 and in revised form 25 October 2004)

The full set of velocity derivatives, $\partial u_i/\partial x_j$, is measured experimentally in a Lagrangian way in quasi-homogeneous isotropic turbulence. This is achieved by applying the three-dimensional particle tracking velocimetry (3D-PTV) technique to an electromagnetically forced flow with $Re_\lambda \approx 50$. Checks based on precise kinematic relations show that the technique presented measures the velocity derivatives with good accuracy. In a study on vorticity, characteristic properties of turbulent flows known from direct numerical simulations are reproduced. These are the positive skewness of the intermediate eigenvalue of the rate of strain tensor, s_{ij}, $\langle \Lambda_2 \rangle > 0$, the predominance of vortex stretching over vortex compression, $\langle \omega_i \omega_j s_{ij} \rangle > 0$ and the predominant alignment of vorticity, $\boldsymbol{\omega}$, with the intermediate principal axis of strain, $\boldsymbol{\lambda}_2$. Results on the evolution in time of material lines, $\boldsymbol{l}$, compared to vortex lines, $\boldsymbol{\omega}$, are presented. They show that the nonlinear interaction of vorticity with the surrounding flow assists viscosity in maintaining this predominant $\boldsymbol{\lambda}_2$-alignment of vorticity. Lagrangian measurements of enstrophy budget terms suggest that there is no pointwise balancing of production and viscous reduction of enstrophy and that the role played by viscosity is of great importance.

1. Introduction

In this paper we report on a first attempt to experimentally measure in a Lagrangian way the full set of velocity derivatives, $\partial u_i/\partial x_j$, with special emphasis on the dynamics of vorticity, $\boldsymbol{\omega} = \operatorname{curl} \boldsymbol{u}$. Despite the fact that the Lagrangian description of fluid flows is physically more natural than the Eulerian one, most turbulence research is still based on Eulerian approaches. This is mainly due to technical difficulties in both laboratory and numerical approaches. With the exception of the work of Tsinober, Kit & Dracos (1992) and Kholmyansky, Tsinober & Yorish (2001) the full set of velocity derivatives, $\partial u_i/\partial x_j$, was up to now accessible only through numerical simulations.

Lagrangian information can be extracted from Eulerian direct numerical simulations (DNS) of the Navier–Stokes equations (NSE) at moderate Reynolds numbers and was reviewed recently by Yeung (2002). These studies were made in simple geometries and emphasized the Lagrangian velocity correlations and accelerations. The work of Girimaji & Pope (1990) is of particular relevance to ours. They performed an extensive numerical study of the behaviour of material elements (lines, surfaces, volumes) in NSE isotropic turbulence, which along with conventional analysis includes the growth rates of material lines and surfaces, deformation of volume elements and alignments with extensive use of the deformation matrix and the Cauchy–Green

tensor. Huang (1996) also addressed similar issues, but in addition made important comparisons between the properties of material lines and those of vorticity such as stretching rates and alignments. Similarly, a comparison between vorticity and passive vectors with the same diffusivity as the fluid viscosity was made by Tsinober & Galanti (2001, 2003) and Ohkitani (2002). Two closely related papers deal with the geometry and evolution of Lagrangian tetrahedrons in quasi-isotropic turbulence: Chertkov, Pumir & Shraiman (1999) and Pumir, Shraiman & Chertkor (2000).

The idea of experimentally tracking neutral tracer particles that approximate the Lagrangian fluid motion was introduced by Snyder & Lumley (1971). Sato & Yamamoto (1987) performed similar experiments in water tunnel grid turbulence. A stereoscopic three-dimensional particle tracking velocimetry (3D-PTV) system was introduced by Chang & Taterson (1983), and was further developed by Racca & Dewey (1988), Maas (1992), Mass, Grün & Papantoniou (1993) and Malik, Dracos & Papantoniou (1993). 3D-PTV was used by Virant & Dracos (1997) in the boundary layer of a free-surface flow, whereas Mann, Ott & Andersen (1999) and Ott & Mann (2000) used a similar system in an oscillating grid turbulence flow. Voth, Satyanarayan & Bodenschutz (1998) and La Porta *et al.* (2001) used silicon strip detectors as optical imaging elements. Most of the above experimental work was concentrated on obtaining the Lagrangian velocity correlations and later accelerations, and studying relative diffusion.

An important recent development was made in the work by Voth, Haller & Gollub (2002). This is the only work in which, along with the velocity field, the field of velocity derivatives and the Cauchy–Green tensor were obtained in a particle tracking experiment. This was achieved by following about 800 fluorescent latex particles of 120 μm in diameter with a sampling rate of 10 Hz, measuring their velocities from the particle trajectories and using polynomial fitting and interpolation of the velocities onto a grid to obtain the velocity as a function of space and time. This is in principle the same procedure as used in our experiments, Lüthi (2002). The main difference – which from a technical point is essential – is that the experiment by Voth *et al.* (2002) was a two-dimensional one, whereas ours is three-dimensional.

Despite the fact that the importance of velocity derivatives was recognized several decades ago by Taylor (1937, 1938) and Kolmogorov (1941*a*, *b*) certain issues regarding vortex stretching and enstrophy, ω^2, dynamics are still not fully understood. Taylor was the first to stress the importance of the positive net enstrophy production, $\langle \omega_i \omega_j s_{ij} \rangle > 0$ in three-dimensional turbulent flows, whereas Kolmogorov emphasized the role of dissipation, $2\nu s_{ij} s_{ij}$ or $2\nu s^2$, and thereby of strain, $s_{ij} = \frac{1}{2}(\partial u_i/\partial x_j + \partial u_j/\partial x_i)$. Since vorticity is a functional of strain and vice versa the evolution of the fields of enstrophy and strain,

$$\frac{1}{2}\frac{\mathrm{D}\omega^2}{\mathrm{D}t} = \omega_i \omega_j s_{ij} + \nu \omega_i \nabla^2 \omega_i \tag{1}$$

and

$$\frac{1}{2}\frac{\mathrm{D}s^2}{\mathrm{D}t} = -s_{ij} s_{jk} s_{ki} - \tfrac{1}{4}\omega_i \omega_j s_{ij} - s_{ij}\frac{\partial^2 p}{\partial x_i \partial x_j} + \nu s_{ij} \nabla^2 s_{ij}, \tag{2}$$

are strongly connected to each other (e.g. Tsinober 2001). The dynamics of velocity derivatives are driven by self-amplification and include two non-locally interconnected weakly correlated processes of enstrophy and strain production (Galanti & Tsinober 2000; Tsinober 2000). The non-locality is discussed in e.g. Novikov (1967), Constantin (1994), Ohkitani & Kishsiba (1995) and Tsinober (2001). The production terms, $\omega_i \omega_j s_{ij}$ and $s_{ij} s_{jk} s_{ki}$, for vorticity and strain are reported to be orders of magnitude

higher than their corresponding terms associated with forcing, Tsinober (2001). There are indications that the process of self-amplification has a universal character for a wide range of different flow types. Manifestations are e.g. maps of the second and third invariants of $\partial u_i/\partial x_j$, R and Q, with their characteristic 'tear-drop' feature (Chacin, Cantwell & Kline 1996; Ooi *et al.* 1999) or characteristic alignments between vorticity and the eigenframe of the rate of strain tensor s_{ij} (Ashurst *et al.* 1987; Constantin 1994; Tsinober *et al.* 1992; Tsinober, Shtilman & Vaisburd 1997; Kholmyansky *et al.* 2001; Lüthi *et al.* 2001, Lüthi 2002).

Trying to explain the positiveness of the strain production term $\langle -s_{ij}s_{jk}s_{ki}\rangle$ of expression (2) is equivalent to explaining the positiveness of $\langle \Lambda_2\rangle > 0$, where Λ_i are the three eigenvalues of s_{ij}, with $\Lambda_1 > \Lambda_2 > \Lambda_3$, and – in incompressible flows – $\Lambda_1 + \Lambda_2 + \Lambda_3 = 0$. With $-s_{ij}s_{jk}s_{ki} = -\Lambda_1\Lambda_2\Lambda_3$ it is clear that the only situation that produces strain is when $\Lambda_2 > 0$. This is what Betchov (1956) calls a jet collision situation. He argues that with the strain produced, vorticity is stretched along $\boldsymbol{\lambda}_1$ and $\boldsymbol{\lambda}_2$ and hence enstrophy is essentially produced through Λ_3. Vortex stretching, $\omega_i\omega_j s_{ij}$, is driven by both vorticity and strain and hence $\langle \Lambda_2\rangle > 0$ is a prerequisite – but no explanation – for positive mean enstrophy production and therefore driving enstrophy dynamics. Enstrophy dynamics as described by expression (1) is governed by the positiveness of $\langle \omega_i\omega_j s_{ij}\rangle$ (e.g. Taylor 1938; Tennekes & Lumley 1972) and the role played by the viscous term $\nu\omega_i\nabla^2\omega_i$. So far, no theoretical arguments in favour of the positiveness of $\langle \omega_i\omega_j s_{ij}\rangle$ have been given. There is evidence that $\langle \omega_i\omega_j s_{ij}\rangle$ would grow without bounds if it were not for viscosity, see Brachet *et al.* (1992). This evidence is based on DNS of the Euler equations. In high-enstrophy regions of viscous flows the mean generation due to predominant vortex stretching is approximately balanced by viscous destruction (Tsinober 2000). It was also shown for a Gaussian field, with $\langle \omega_i\omega_j s_{ij}\rangle$ identically zero at time $t = 0$, that within a very short time interval the mean enstrophy production will become positive, $(\mathrm{D}/\mathrm{D}t)\langle \omega_i\omega_j s_{ij}\rangle > 0$, see Proudman & Reid (1954).

One of the common views is that the prevalence of vortex stretching is due to the predominance of stretching of material lines (Taylor 1938). This view is widely accepted, e.g. in Hunt (1973); however, it is at best only partially true, since there exist several essential qualitative differences between the two processes. From comparison of the equations for vorticity

$$\frac{\mathrm{D}\omega_i}{\mathrm{D}t} = \omega_j\frac{\partial u_i}{\partial x_j} + \nu\nabla^2\omega_i \tag{3}$$

and

$$\frac{\mathrm{D}l_i}{\mathrm{D}t} = l_j\frac{\partial u_i}{\partial x_j} \tag{4}$$

for material line elements, $\boldsymbol{l}$, it is clear that the evolution of vorticity is nonlinear whereas material lines evolve in a purely kinematic manner. In addition vortex lines are influenced by viscous effects which allow reconnection phenomena (Kida & Takaoka 1994; Fernandez, Zabusky & Gryanik 1995) and which are responsible for balancing the enstrophy production of the term $\omega_i\omega_j s_{ij}$. A detailed list of differences between material lines and vortex lines is given in Tsinober (2001). Among the key differences between vortex and material lines is their different predominant alignment with respect to the eigenframe of strain $\boldsymbol{\lambda}_2$ and $\boldsymbol{\lambda}_1$ respectively (Dresselhaus & Tabor 1991; Huang 1996; Lüthi *et al.* 2001, Lüthi 2002).

One important consequence of the predominant $\boldsymbol{\omega}$–$\boldsymbol{\lambda}_2$ alignment is that growth of enstrophy production is moderated and bounded through dynamic interaction with strain and through viscous processes, whereas material line energy experiences unbounded growth. It is the aim of this paper to focus on the mechanisms that are involved in controlling the evolution of $\omega_i\omega_j s_{ij}$. We will obtain a picture of a field of vorticity that has self-regulating growth, equilibrium and reduction of enstrophy, through dynamical interaction with strain and through viscosity. The essential prerequisite for such a study is the 3D-PTV technique presented which allows active and passive vectors $\boldsymbol{l}$ and $\boldsymbol{\omega}$ to be measured in a Lagrangian way, as well as enstrophy budget terms like $\frac{1}{2}(\mathrm{D}\boldsymbol{\omega}^2/\mathrm{D}t)$ and $\omega_i\omega_j s_{ij}$, along particle trajectories.

The paper is organized as follows: In § 2 the experimental setup and the technique of obtaining the velocity gradient tensor $U_{ij} = \partial u_i/\partial x_j$ by means of 3D-PTV is outlined and verified. In § 3 we demonstrate that with 3D-PTV measurements most relevant results regarding the fine-scale structure of isotropic turbulence, known from DNS studies (e.g. Siggia 1981; Ashurst *et al.* 1987; Girimaji & Pope 1990; Vincent & Meneguzzi 1994; Huang 1996; Tsinober 2001; Tsinober & Galanti 2001, 2003) and hot-wire experiments (Tsinober *et al.* 1992; Kholmyansky *et al.* 2001) can be reproduced. In § 4 we move on from Eulerian to essentially Lagrangian results. Through the study of special material lines we identify how $\boldsymbol{\omega}$ can stabilize its $\boldsymbol{\lambda}_2$-alignment and we investigate the point-wise relation between the enstrophy terms $\frac{1}{2}(\mathrm{D}\boldsymbol{\omega}^2/\mathrm{D}t)$ and $\omega_i\omega_j s_{ij}$ and its implications for the viscous term $\nu\omega_i\nabla^2\omega_i$. In § 5 the results are summarized and some conclusions are drawn.

2. Experimental setup and measurement

2.1. *Flow*

The flow domain is a rectangular box, $120 \times 120 \times 140\,\mathrm{mm}^3$, with the flow forced electromagnetically by Lorentz forces, $\boldsymbol{f}_L$, from two opposite walls,

$$\boldsymbol{f}_L = \boldsymbol{j} \times \boldsymbol{B}, \tag{5}$$

where $\boldsymbol{j}$ is the current density and $\boldsymbol{B}$ the magnetic field. To reach a high electrical conductivity and hence current density $\boldsymbol{j}$, a saturated copper sulphate ($CuSO_4$) solution is used as fluid. The fluid has a conductivity of $16.7\,\mathrm{mS\,cm^{-1}}$, a density, ρ, of $1050\,\mathrm{kg\,m^{-3}}$, and a dynamic viscosity, ν, of $1.2 \times 10^{-6}\,\mathrm{m^2\,s^{-1}}$. For the magnetic field at each wall a 2×2 array of cylindrical rare-earth strong permanent magnets are used. They have a diameter of 42 mm, an axial length of 20 mm, and a strength, $\boldsymbol{B}$, of over 1 T. The interaction of the wall-normal current density field, $\boldsymbol{j} = 70\,\mathrm{A\,m^{-2}}$, with the magnetic field leads to volumetric forcing which is tangential, with respect to the axis of the magnets, and is strongest in a torus-like region above the magnets reaching up to 5 mm into the flow. The forcing produces a non-oscillating swirling motion in the proximity of each magnet. The magnets are arranged in such a way that the resulting swirls are analogous to a 'milling' flow in the laminar situation. Within a few seconds these swirls cause a three-dimensional time-dependent flow region with a front that quickly propagates towards the centre resulting in a turbulent velocity field with zero mean flow and fluctuations, u_i, of $O(0.01\,\mathrm{m\,s^{-1}})$, occupying the entire volume of the tank. This type of non-oscillating forcing has the advantage that it is confined to large scales and that it introduces no time scales which might be remembered throughout the flow's history. Also, it introduces no mechanical vibrations. Simple systems of such a kind have been successfully used since the 1970s by the group of A. Obukhov

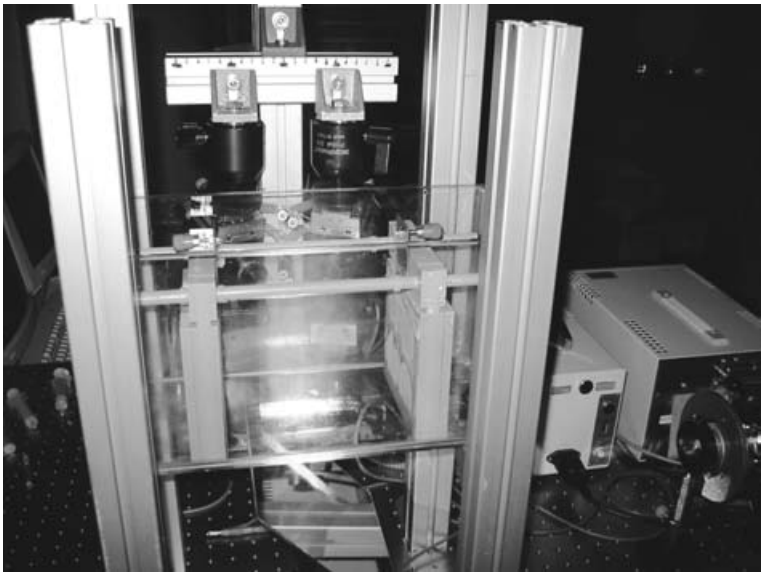

FIGURE 1. Experimental setup. The flow is produced with electromagnetic forcing. The observation volume is illuminated with a continuous argon-ion laser and recorded with four CCD cameras.

(e.g. Obukhov 1983; Cardoso *et al.* 1996; Honji, Ohkura & Ikehata 1997) with simple quasi-two-dimensional flows and by Yule (1975) who has used electromagnetic forcing of low Reynolds number flow in a pipe.

The flow is seeded with neutrally buoyant 40 μm polystyrene particles. In each time step ~ 800 particles are detected and can be allocated a position in space. With an observation volume of $20 \times 15 \times 15\,\mathrm{mm}^3$ this corresponds roughly to a particle seeding density of ~ 180 particles cm^{-3}. The effective seeding density of particles that can be followed long enough in time so that they will enter into the interpolation scheme is of course lower, as will be outlined further below. For illumination a continuous 20 W argon ion laser is used. The laser beam is widened by two cylindrical lenses to a laser sheet of 20 mm thickness. The flow is recorded with four CCD progressive scan monochrome cameras with $8\,\mathrm{bit\,pixel}^{-1}$ and 640×480 pixels resolution. In our experiment a target with 36 points distributed in a volume of $18 \times 15 \times 7\,\mathrm{mm}^3$ is used for camera calibration. Following the procedures extensively described in Maas *et al.* (1993), Virant (1996) and Stüer (1999) the estimated position accuracy for the target points is ~ 3 μm leading to an estimated position accuracy of the fluid tracer particles of ~ 10 μm for the x and y components and ~ 40 μm for z. This reflects that because of the way the four cameras are set up, determination of a particle's z position is the most difficult. Changing camera position and angles in favour of equal particle position accuracy for all three components would in turn reduce the volume where all four fields of view with corresponding depth of field overlap. The particle position accuracy is somewhat lower than target point accuracy due to combined effects of particle size, illumination and motion. The synchronized images are stored on two PCs with 4 GB RAM memory each at a frame rate of 60 Hz. The system records at $72\,\mathrm{MB\,s}^{-1}$ over 100 s which corresponds to a total of 6000 frames. The setup of the experiment is shown in figure 1.

2.2. *Three-dimensional particle tracking velocimetry*

The three-dimensional particle tracking velocimetry (3D-PTV) technique is a flexible non-intrusive image-analysis-based flow measurement technique. It measures particle trajectories from which – if the particles are neutrally buoyant and small enough to perfectly follow the flow – particle velocities and Lagrangian accelerations can be obtained directly.

3D-PTV can be divided into two major parts: determination of particle positions in spatial coordinates and tracking of individual particles through consecutive images. While in previous implementations these two steps had been completely separated Willneff (2003) combined the two steps and developed a new spatiotemporal matching method which improves tracking efficiency of particles by 10–30%. Until then, the probability of position and tracking ambiguities could only be reduced by using low particle seeding densities with the negative effect of drastically reducing spatial resolution, which in turn made determination of velocity derivatives impossible. Willneff's new idea was to exploit the redundant information in image and object space more effectively. Predictions of particle motion, based on particle tracking in image and object space, are used to resolve ambiguous particle image positions and correspondences. In other words, 'temporal' information at time, t, is used to resolve 'spatial' uncertainties regarding the existence and positions of particles in the next time step $t + \Delta t$. The seemingly modest improvement of 10–30% in tracking efficiency is very significant in the context of further processing and analysis. Very often trajectories are lost due to small gaps over one or two frames where trajectory paths cross in image planes leading to unsolved ambiguities. The spatiotemporal matching method is found to be particularly efficient in closing these gaps which has as a consequence that the number of long trajectories is more than doubled. Particle trajectories which are longer than the relevant Kolmogorov scales, η, and τ_η, are the key prerequisite for a Lagrangian flow analysis and, as we will show below, they also significantly enhance the accuracy of the applied processing to obtain velocity derivatives.

To track particles, i.e. to find corresponding particles in image and object space of consecutive time steps, three criteria are used for effective assignment. First, a three-dimensional search volume is defined by minimum and maximum velocities in all three coordinate directions. Second, the Lagrangian acceleration of a particle is limited, defining a conic search area. Third, in the case of ambiguities the particle leading to the smallest Lagrangian acceleration is chosen. Similarities in brightness, width, height and sum of grey values of the pixel of a particle image in two consecutive time steps proved to be not as valuable as expected. From the 800 detected particles per frame for which a position in space can be determined, typically 470 particles can be followed long enough, which is equivalent to a tracking efficiency of $\sim$60% and a seeding density for linked particles of $\sim$105 particles cm^{-3}. 'Long enough' means that particle positions along trajectories can be fitted to a moving cubic polynomial, which acts as a low-pass filter. With the fitting procedure, filtered positions, $\widehat{\boldsymbol{x}}$, filtered velocities, $\widehat{\boldsymbol{u}}$, and filtered accelerations, $\widehat{\boldsymbol{a}}$, are assigned to each particle. The low-pass filtering and its characteristics are described in Appendix A. As a qualitative illustration of the result of the tracking procedure figure 2 shows recorded trajectories from the beginning of an experiment that can be tracked over 0.3 s or longer.

2.3. *Velocity derivatives*

From the technical point of view this section is the most important one, since it describes how the full set of spatial and temporal velocity derivatives, $\partial u_i/\partial x_j$ and

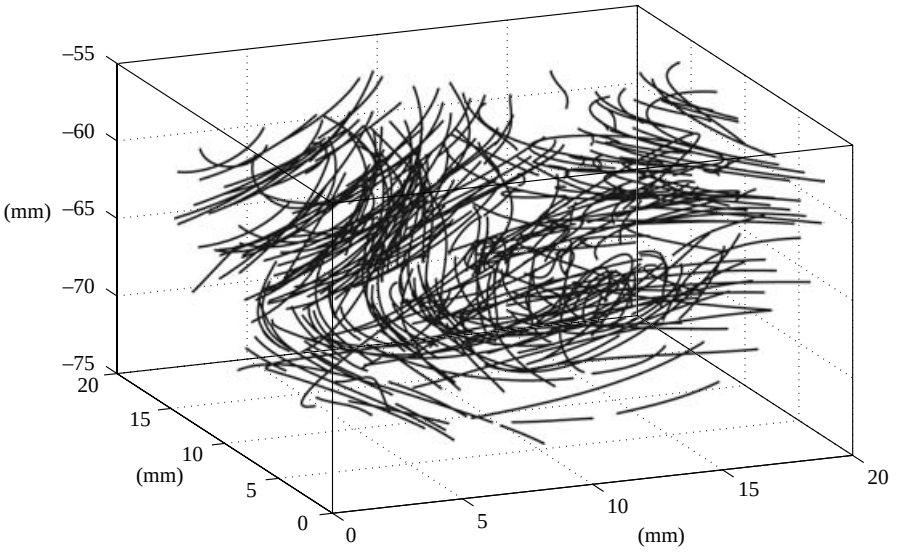

FIGURE 2. Selected particle trajectories as obtained from 3D-PTV.

$\partial u_i/\partial t$, are obtained for every point $\boldsymbol{x}$ along particle trajectories from information on velocities, $\widehat{\boldsymbol{u}}$, in the proximity of $\boldsymbol{x}$. The procedure involves two steps: a local linear interpolation of the velocity field and a weighted polynomial fit to the derivatives along particle trajectories, making use of the auto-correlations of the Lagrangian derivatives. The weighting in the last step is crucial, since it allows contributions to the fit to such trajectory to be confined to data where a local quality estimation, based on divergence, suggests that the interpolated derivatives are sufficiently accurate.

2.3.1. *Linear interpolation*

From low-pass filtered velocities, $\widehat{u_i}$, spatial and temporal velocity derivatives are interpolated for every particle trajectory point. The details of the low-pass filtering are outlined in Appendix A. Assuming that to a good approximation the velocity field in the proximity of position $\boldsymbol{x}_0$ is linear, for $\widehat{u_i}(\boldsymbol{x}_0)$, $i = 1, 2, 3$, the linear ansatz

$$\widehat{u_i}(\boldsymbol{x}_0) = c_{i,0} + c_{i,1}x_1 + c_{i,2}x_2 + c_{i,3}x_3, \tag{6}$$

with

$$c_{i,1} = \frac{\partial u_i}{\partial x_1}, \quad c_{i,2} = \frac{\partial u_i}{\partial x_2}, \quad c_{i,3} = \frac{\partial u_i}{\partial x_3}$$

is made. In principal, information from four points, $n = 4$, is sufficient to solve expression (6) for $\boldsymbol{c}_i$. Since the sensitivity of $c_{i,j}$ to errors of $\widehat{u_i}$ is high, an over-determined linear system,

$$\boldsymbol{A}\boldsymbol{c}_i = \boldsymbol{v}_i, \tag{7}$$

with information from n points, $n > 4$, is desirable. Given that all n points are close enough for the linear ansatz to remain valid, the confidence interval for $c_{i,j}$ improves with $\sim (n)^{-1/2}$. Expression (7) is solved for c_i with the least-square method as

$$\boldsymbol{c}_i = (\boldsymbol{A}^T\boldsymbol{v}_i)(\boldsymbol{A}^T\boldsymbol{A})^{-1}, \tag{8}$$

where $\boldsymbol{A}$ is the position matrix and $\boldsymbol{v}_i$ is the velocity vector.

The spatial separation over which to a good approximation the velocity field may be linearized is not known *a priori*. It will be limited, however, to separations

	particle frame^{-1}	particle cm^{-3}	%
Detected, x	800	180	100
Low-pass filtered, $\widehat{u}$, $\widehat{a}$	470	105	59
Fully processed, $\partial u/\partial x$, $\partial u/\partial t$	190	42	23

TABLE 1. Effect of the procedure on particle seeding density.

for which viscous effects are dominant, and thus where velocity fields are much more likely to be covered by a low-order ansatz. An upper bound for the viscous subrange separations, s_ν, is estimated indirectly and found to be $s_\nu < 4\,\text{mm}$. The derivation of s_ν is described in Appendix B. $s_\nu < 4\,\text{mm}$ results in a typical number of interpolation points of $n \approx 20$. This is equivalent to an effective seeding density for linked particles that actually enter the procedure for determining velocity derivatives of $\sim 20(4/3 \times \pi \times 0.4^3)^{-1} \sim 75\,\text{particles}\,\text{cm}^{-3}$.

Temporal velocity derivatives are obtained analogously with the ansatz

$$\widehat{u_i}(\boldsymbol{x}_0) = c_{i,0} + c_{i,1}x_1 + c_{i,2}x_2 + c_{i,3}x_3 + c_{i,4}t. \tag{9}$$

Here information from points with $r < 4\,\text{mm}$ from times t and $t \pm 2\Delta t$, $\Delta t = 1/60\,\text{s}$, are used.

2.3.2. *Weighted fit along particle trajectories*

It is clear that in a situation with large second velocity derivatives the spatial validity of the linear expression (6) is smaller than that of the estimate obtained. This will ultimately result in a poor approximation for $\partial u_i/\partial x_j$ and $\partial u_i/\partial t$ and needs to be corrected for. Using the fact that $\partial u_i/\partial x_j$ and $\partial u_i/\partial t$ are – to some extent – auto-correlated along their trajectory paths, again a procedure that effectively acts as a low-pass filter is applied. Polynomials of type

$$\frac{\partial u_i}{\partial x_j}(t),\ \frac{\partial u_i}{\partial t}(t) = \sum_{k=0}^{n} c_k\, t^k \tag{10}$$

and of adequate order, n, are fitted to each velocity derivative signal, $\partial u_i/\partial(\cdot)$, along the entire trajectory of length, ℓ, where the contribution of every particle trajectory point is weighted according to the local quality of the linear interpolation. As a measure for the local interpolation quality a relative divergence, δ, is defined as

$$\delta = \frac{\|\partial u_1/\partial x_1 + \partial u_2/\partial x_2 + \partial u_3/\partial x_3\|}{\|\partial u_1/\partial x_1\| + \|\partial u_2/\partial x_2\| + \|\partial u_3/\partial x_3\|}. \tag{11}$$

Using δ from expression (11) for weighting, the incompressibility of water which has not yet been used enters the procedure and assists in recovering velocity derivative signals. The details of the fitting are outlined in Appendix C. As will be shown in the next section on verification, in particular the use of weighted contributions to the polynomial fit yields a significant improvement of the velocity derivative signals obtained.

At the end of the full procedure we have $p \sim 1 \times 10^6$ data points stemming from 6000 frames that belong to a trajectory of length $\ell > 15$ and for which the full set of velocity derivatives can be derived with a quality of $\delta < 0.1$. Table 1 gives an overview of how many of the initially detected particles survive which steps of the described procedure.

	$\sqrt{\overline{u_i^2}}$	$\sqrt{\overline{(\partial u_i/\partial x_i)^2}}$	$\lambda_i = \sqrt{\dfrac{\overline{u_i^2}}{\overline{(\partial u_i/\partial x_i)^2}}}$
$i=1$	$6.5\,\mathrm{mm\,s^{-1}}$	$1.05\,\mathrm{s^{-1}}$	6.19 mm
$i=2$	$5.5\,\mathrm{mm\,s^{-1}}$	$0.90\,\mathrm{s^{-1}}$	6.11 mm
$i=3$	$6.4\,\mathrm{mm\,s^{-1}}$	$1.01\,\mathrm{s^{-1}}$	6.33 mm

	$15\nu\overline{(\partial u_1/\partial x_1)^2}$	$15\nu\overline{(\partial u_2/\partial x_2)^2}$	$15\nu\overline{(\partial u_3/\partial x_3)^2}$	$2\nu\overline{s_{ij}s_{ij}}$
$\varepsilon\,(\mathrm{mm^2\,s^{-3}})$	20	15	19	16
$\eta\,(\mathrm{mm})$	0.54	0.58	0.55	0.57
$\tau_\eta\,(\mathrm{s})$	0.25	0.28	0.25	0.27

TABLE 2. Characteristic properties of the flow.

2.3.3. *Characteristic properties and scales*

In table 2 the characteristic properties and scales for the flow are given. η is defined as

$$\eta = \left(\frac{\upsilon^3}{\varepsilon}\right)^{1/4}, \tag{12}$$

and its corresponding time scale, τ_η, as

$$\tau_\eta = \left(\frac{\upsilon}{\varepsilon}\right)^{1/2}.$$

The Taylor Reynolds number is obtained as

$$Re_\lambda = \frac{\sqrt{\overline{u^2}}\lambda}{\nu} \sim 50 \tag{13}$$

with

$$\sqrt{\overline{u^2}} = \sqrt{\overline{u_i^2} + \overline{u_2^2} + \overline{u_3^2}} \sim 10\ (\mathrm{mm\,s^{-1}}). \tag{14}$$

The 6000 frames recorded are equivalent to 380 Kolmogorov time scales τ_η, $\tau_\eta = 0.26\,\mathrm{s}$, with a temporal resolution of 15 frames per τ_η. The trajectories recorded cover a volume of $36 \times 27 \times 27\,\eta^3$ ($\eta = 0.55\,\mathrm{mm}$). A close inspection of the data shows that most trajectories begin and end close to the boundary of the observation domain and that only a small percentage of particle trajectories is lost during their residence in the domain. This results in a slight bias towards shorter trajectories, since they have a shorter residence time in the mean.

2.4. *Verification*

The final quality of the velocity derivatives is assessed by looking at the behaviour of the two quantities $\langle\delta\rangle$ and $\langle\boldsymbol{\omega}^2\rangle/\langle s^2\rangle$ as functions of particle trajectory lengths, ℓ, and with checks based on precise local kinematic relations. By doing this, both the quality of the data itself and the beneficial influences of the post-processing procedures described above is demonstrated. From the kinematic checks the accuracy of the terms $\partial u_i/\partial x_j$ is obtained which later will be used to approximate accuracies for higher-order terms, such as $\frac{1}{2}(\mathrm{D}\boldsymbol{\omega}^2/\mathrm{D}t)$, and $\omega_i\omega_j s_{ij}$. At the end of this section we demonstrate that not only is the accuracy of the filtered data adequate, but that also the filtered data are still representative of the entire flow, e.g. that the filtered data are not biased towards low-intensity flow events.

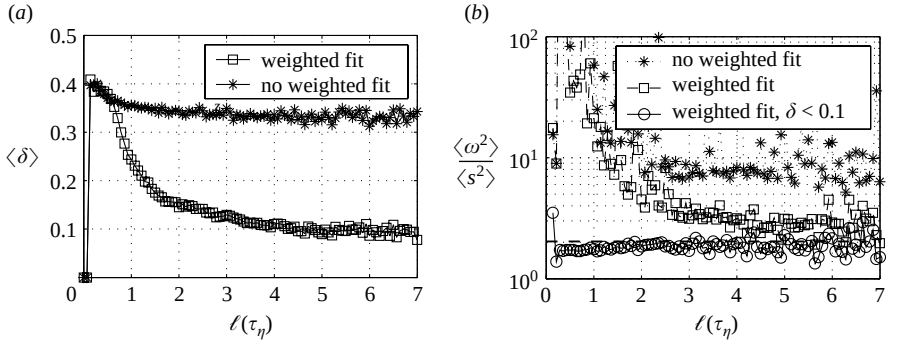

FIGURE 3. (*a*) Relative divergence $\langle\delta\rangle$ plotted over trajectory length ℓ. (*b*) Ratio of mean enstrophy, ω^2, over mean strain, s^2, plotted over ℓ.

2.4.1. *Checks*

We begin with two checks that reveal the influence of the measured trajectory length, ℓ, on the quality of the interpolation procedure for $\partial u_i/\partial x_j$. We first show the mean relative divergence, $\langle\delta\rangle$, as defined in expression (11), plotted as a function of ℓ in figure 3(*a*). The use of the weighted fitting procedure results in a $\langle\delta\rangle$ that after a delay of $\ell \approx 0.5\tau_\eta$ starts to decay towards 0.1, whereas $\langle\delta\rangle$ derived from $\partial u_i/\partial x_j$ without weighted fitting remains at a high level of over 0.3. This demonstrates the effectiveness of the procedure and that its full impact is only reached for trajectories with $\ell > \tau_\eta$. The delay, which is equivalent to 8 frames ($\tau_\eta = 0.26$ s, table 2), can be explained by considering that in our experiment on average 40% of the interpolated points are of high quality, i.e. $\delta < 0.1$. A fit of third order to derive four constants requires a minimum of $n = 4 \times (40\%)^{-1} = 10$ or even more points to result in a 'good' fit, i.e. a fit with low overall δ.

Further, we show in figure 3(*b*) the quantity $\langle\boldsymbol{\omega}^2\rangle/\langle s^2\rangle$ plotted as a function of the trajectory length ℓ. In homogeneous turbulence the relation

$$\langle\boldsymbol{\omega}^2\rangle = 2\langle s^2\rangle$$

is valid (Tennekes & Lumley 1972) and therefore should also be recovered with our measurements. However in figure 3(*b*) only the fully processed data that are conditioned on $\delta < 0.1$ converge to the theoretically correct ratio of $\langle\boldsymbol{\omega}^2\rangle/\langle s^2\rangle = 2$. Unconditioned data obtained from the weighted fitting procedure $\langle\boldsymbol{\omega}^2\rangle/\langle s^2\rangle$ reach a stable but slightly too high value only for $\ell > 3$. It appears that this is caused by too low estimates for strain values which reach their proper magnitude only after being fully processed, contrary to enstrophy which in turn is overestimated without the full processing.

In the 'divergence check' due to incompressibility of water ideally the trace of $\partial u_i/\partial x_j$ should be zero, i.e.

$$-\frac{\partial u_i}{\partial x_i} = \frac{\partial u_j}{\partial x_j} + \frac{\partial u_k}{\partial x_k}. \tag{15}$$

Joint PDFs of $-\partial u_i/\partial x_i$ versus $\partial u_j/\partial x_j + \partial u_k/\partial x_k$ (with no summation over i, j, k applied) are shown in figure 4 for two cases: the fully processed data and data 'as obtained' from linear interpolation only. Ideally all data should fall onto the diagonal. However, taking into account that the measured and filtered $\partial u_i/\partial x_j$ are comprised of $(\partial u_i/\partial x_j)_{exact}$ plus some error, $\varepsilon_{\partial u_i/\partial x_j}$, the joint PDFs can be expected to have

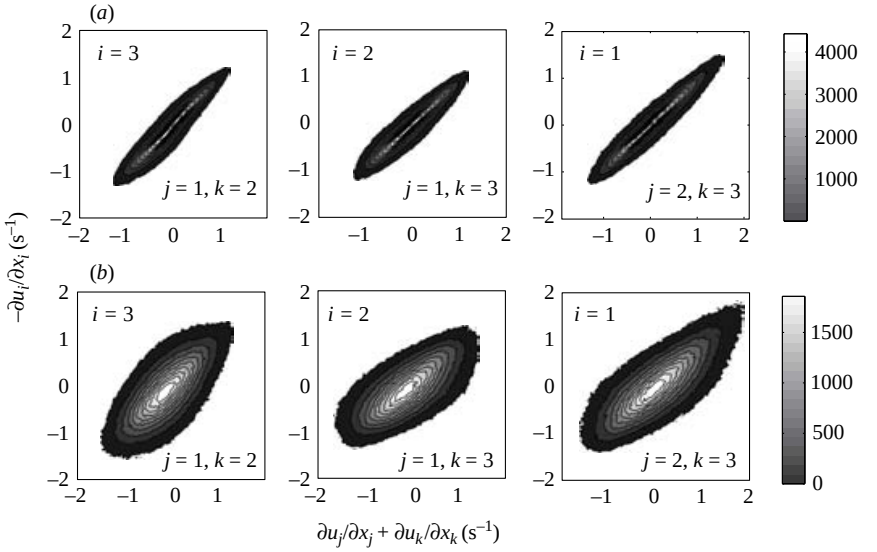

FIGURE 4. Joint PDFs of $-\partial u_i/\partial x_i$ versus $\partial u_j/\partial x_j + \partial u_k/\partial x_k$ (here no summation over i, j, k is applied) for two cases, as obtained from linear interpolation: (a) with and (b) without the weighted fitting procedure.

elliptical contour shapes with aspect ratios of $1/n$. Assuming that $1/n$ is reflecting the relative error of $\partial u_i/\partial x_j$ we approximate $\varepsilon_{\partial u_i/\partial x_j}$ as

$$\varepsilon_{\partial u_i/\partial x_j} = \frac{\mathrm{rms}(\partial u_i/\partial x_j)}{\sqrt{2}n}. \tag{16}$$

Figures 4(a) and 4(b) show for the fully processed case and derivatives obtained from linear interpolation elliptical contours with aspect ratios of 1/5 and 1/2.6 respectively. With a measured $\mathrm{rms}(\partial u_i/\partial x_j) \sim 1\,\mathrm{s}^{-1}$ (table 2) this implies that the error relative to its r.m.s. is reduced from

$$\varepsilon_{\partial u_i/\partial x_j} = \frac{1\,\mathrm{s}^{-1}}{\sqrt{2}\times 2.6} = 0.27\,\mathrm{s}^{-1} = 27\% \tag{17}$$

by almost a factor 2 to

$$\varepsilon_{\partial u_i/\partial x_j} = \frac{1\,\mathrm{s}^{-1}}{\sqrt{2}\times 5} = 0.14\,\mathrm{s}^{-1} = 14\% \tag{18}$$

by applying the weighted fitting procedure to the data obtained from linear interpolation. The fact that joint PDF contours are similar from column to column and that they are all centred around the origin shows that the flow – on the level of spatial velocity derivatives – is isotropic. Taking a closer look at the behaviour of the velocity component $\partial u_3/\partial x_3$ we note that all contour shapes which already have a relatively low aspect ratio are 'stretched' along the axis where $\partial u_3/\partial x_3$ is involved. Due to camera angles this component is more difficult to measure. Comparing figure 4(b) to figure 4(a) shows how inaccurate $\partial u_3/\partial x_3$ signals stemming from inaccurate x_3 positions are corrected by the weighted polynomial fitting procedure, without damping the overall magnitude of the components of $\partial u_i/\partial x_i$. This is a first indication that the weighted polynomials enhance the quality of the measured and interpolated components of $\partial u_i/\partial x_j$.

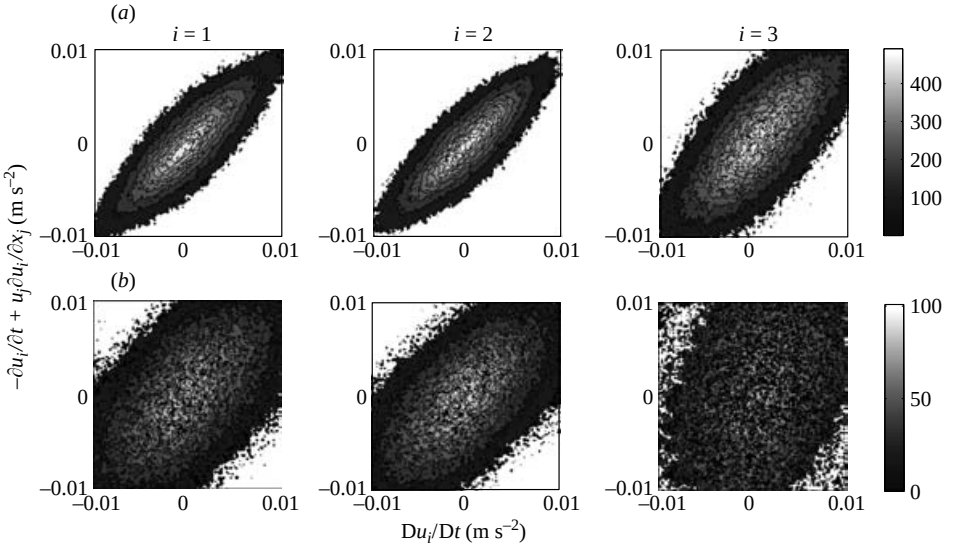

FIGURE 5. The expression $Du_i/Dt = \partial u_i/\partial t + u_j \partial u_i/\partial x_j$ is checked for each component with joint PDFs of $a_{l,i} + a_{c,i}$ versus a_i for the two cases (a) with and (b) without the weighted fitting procedure.

The next check involves all quantities that were measured: Lagrangian accelerations, $a_i = Du_i/Dt$, local accelerations, $a_{l,i} = \partial u_i/\partial t$, and convective accelerations, $a_{c,i} = u_j \partial u_i/\partial x_j$. Since each of these quantities is derived in a different manner they make an excellent, though hard to pass, overall check of the applied procedures, i.e.

$$\frac{Du_i}{Dt} = \frac{\partial u_i}{\partial t} + u_j \frac{\partial u_i}{\partial x_j}. \tag{19}$$

In figure 5 expression (19) is checked for each component with joint PDFs of a_i versus $a_{l,i} + a_{c,i}$ for data with relative divergence $\delta < 0.1$. The emerging picture is similar to the one obtained from the divergence check: the use of the weighted polynomial fitting procedure strongly enhances the accuracy of velocity derivatives. The aspect ratios of the contour shapes are lower than those of figure 4, reflecting the higher standard of this kind of check. The effect of the x_3-component inaccuracy is much more pronounced in figure 5 than in figure 4. Through the use of weighted polynomial fits it can only be corrected up to a certain degree. The PDFs of figure 5(b) show a slight misalignment of the contours relative to the diagonal for $i = 1$ and $i = 2$ and a large misalignment for $i = 3$. It is likely that this is caused by a systematic overestimation of the magnitudes of a_l and a_c compared to a. The derivation of a_l and a_c involve a much more complicated procedure than the Lagrangian acceleration a, which is obtained in a relatively straightforward manner.

Assuming that the errors of $a_{l,i}$ and $a_{c,i}$ are of equal order of magnitude and that the error for a_i is small compared to its local and convective components,

$$O\left(\varepsilon_{a_{l,i}}\right) \approx O\left(\varepsilon_{a_{c,i}}\right) > O\left(\varepsilon_{a_i}\right), \tag{20}$$

the above result allows one to verify the following approach that theoretically approximates errors (also for higher-order quantities). Formally the error $\varepsilon_{a_{c,i}}$ can be defined as

$$\varepsilon_{a_{c,i}} = (u_j + \varepsilon_u)\left(\frac{\partial u_i}{\partial x_j} + \varepsilon_{\partial u_i/\partial x_j}\right) - a_{c,i}. \tag{21}$$

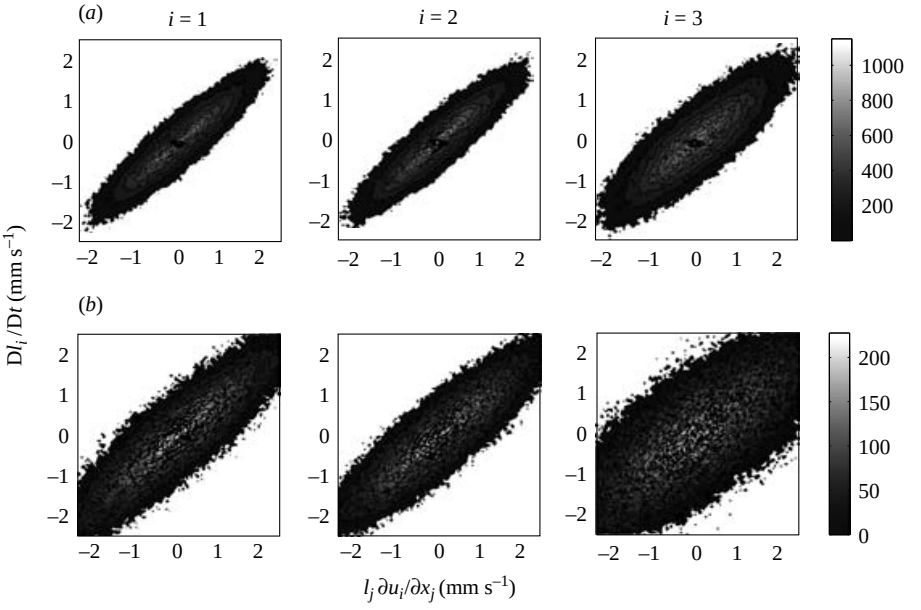

FIGURE 6. The expression $\mathrm{D}l_i/\mathrm{D}t = l_j \partial u_i/\partial x_j$ is checked for each component with joint PDFs of $\mathrm{D}l_i/\mathrm{D}t$ versus $l_j \partial u_i/\partial x_j$ for the two cases (*a*) with and (*b*) without the weighted fitting procedure.

With a particle position inaccuracy ε of 0.01 mm for the x and y components and 0.04 mm for the z component respectively, the velocity error ε_u is approximately

$$\varepsilon_u \approx \frac{0.01..0.04}{\Delta t}(21/4)^{-1/2} \approx 0.5\,\mathrm{mm\,s^{-1}}, \tag{22}$$

when we assume that a 21 point fit to a cubic polynomial with four constants reduces the error by $(21/4)^{-1/2}$. Summing (21) over j, with $\varepsilon_u \approx 0.5\,\mathrm{mm\,s^{-1}}$ and $O(u_j) \approx 6\,\mathrm{mm\,s^{-1}}$, $O(\partial u_i/\partial x_j) \approx 1\,\mathrm{s^{-1}}$ from table 2, and $\varepsilon_{\partial u_i/\partial x_j} \approx 0.14\,\mathrm{s^{-1}}$ from (18), expression (21) yields

$$\varepsilon_{a_{c,i}} = 3\left[O(u_j)\varepsilon_{\partial u_i/\partial x_j} + \varepsilon_u\, O\left(\frac{\partial u_i}{\partial x_j}\right)\right] = 4\,\mathrm{mm\,s^{-2}}. \tag{23}$$

To compare this result with the measurements we use the aspect ratios $1/n$ of the contours of figure 5 in analogy with expression (16). $\varepsilon_{a_{c,i}}$ can be defined as

$$\varepsilon_{a_{c,i}} = \frac{\mathrm{rms}(a_{c,i})}{\sqrt{2}n}. \tag{24}$$

With $\mathrm{rms}(a_{c,i}) = 14\,\mathrm{mm\,s^{-2}}$ and $n = 3.5$ we find $\varepsilon_{a_{c,i}} = 2.8\,\mathrm{mm\,s^{-2}}$ – which is equivalent to a relative error of 20%. Thus, the error actually measured is found to not only agree well with the theoretically derived error (expression (23)), but further, it is only 70% of its value. This suggests that the restriction to data points where divergence is low and $\delta < 0.1$ yields decrease of error by a factor 0.7.

The next check is on material lines. In figure 6 joint PDFs of $\mathrm{d}l_i/\mathrm{d}t$ and $l_j \partial u_i/\partial x_j$ are plotted for each component. This check is of special importance since it shows whether or not the flow is adequately resolved by the proposed 3D-PTV method. It directly tests whether expression (4) is met. Here $\mathrm{d}l_i/\mathrm{d}t$ and l_j are material lines

between two measured tracer particles that initially are separated by no more than 3.5 mm. If one finds that the joint PDFs of $\mathrm{d}l_i/\mathrm{d}t$ and $l_j \partial u_i/\partial x_j$ roughly fall onto a diagonal then two things are verified. First, it implies that 3.5 mm separations are still close to the linear or viscous subrange separation. This is important because the interpolations are performed with points from within a sphere of $r = 4$ mm. Second, if the measured $\partial u_i/\partial x_j$ is capable of predicting the evolution of such l, then this proves that the spatial resolution of the flow is adequate. From figure 6 – which again demonstrates the beneficial impact on accuracy of the full procedure – we read off aspect ratios for the elliptical contours of 1/4. This results in a measured accuracy for $l_{c,i} = l_j \partial u_i/\partial x_j$ relative to its r.m.s. of

$$\varepsilon_{l_{c,i}} = \frac{\mathrm{rms}(l_{c,i})}{n} = \frac{3.5\,\mathrm{mm\,s^{-1}}}{4} = 0.9\,\mathrm{mm\,s^{-1}} = 25\%. \tag{25}$$

This is identical to the theoretical estimate

$$\varepsilon_{l_{c,i}} = (l_j + \varepsilon_l)\left(\frac{\partial u_i}{\partial x_j} + \varepsilon_{\partial u_i/\partial x_j}\right) - l_{c,i}, \tag{26}$$

for which we also find

$$\varepsilon_{l_{c,i}} = 0.7 \times 3\left[O(l_j)\,\varepsilon_{\partial u_i/\partial x_j}\right] = 0.9\,\mathrm{mm\,s^{-1}} = 25\%, \tag{27}$$

with the factor 0.7 taking into account data restriction to $\delta < 0.1$, $O(l_j) \approx 3$ mm and $\varepsilon_l \ll 1$.

Assuming that velocity gradients in turbulence are bounded, an initially infinitesimal material element remains infinitesimal for a finitely long time and during this period the velocity gradients can be considered uniform over the material element. This provides a useful alternative way to study the evolution of infinitesimal elements by means of a one-point description of the velocity gradients by following a single particle along its trajectory. Referring to Monin & Yaglom (1997), an infinitesimal material line element which is initially $\boldsymbol{l}(0)$, is given at any later time, t, by

$$\boldsymbol{l}(t) = \boldsymbol{B}(t) \cdot \boldsymbol{l}(0), \tag{28}$$

where $\boldsymbol{B}$ evolves according to the equation

$$\frac{\mathrm{d}}{\mathrm{d}t}\boldsymbol{B} = \boldsymbol{h}(t) \cdot \boldsymbol{B}(t), \qquad \boldsymbol{h}(t) = \left(\frac{\partial u_i}{\partial x_j}\right)_t, \tag{29}$$

with the initial condition $\boldsymbol{B}(0) = \boldsymbol{I}$ and $\boldsymbol{I}$ the identity matrix. As a validation that the integration in time of $\boldsymbol{B}$, for which a third-order Runge–Kutta scheme is used, is correct we show in figure 7(a) the mean logarithmic eigenvalues, $\langle w_i \rangle$, of the Cauchy–Green Tensor $\boldsymbol{W} = \boldsymbol{B}\boldsymbol{B}^T$. An ellipsoid with initial axis ratios of 1 : 1 : 1 will deform into an ellipsoid with axis ratios of $\sqrt{w_1} : \sqrt{w_2} : \sqrt{w_3}$. Due to incompressibility the volume, V, is conserved and with $V = 1$ we have

$$\ln(w_1) + \ln(w_2) + \ln(w_3) = 0. \tag{30}$$

From figure 7(a) which is in full agreement with results of Girimaji & Pope (1990) we see that expression (30) is met for all times. Further, we note that fluid volumes are not only stretched along the principal axis but also along the intermediate axis of $\boldsymbol{W}$.

A stronger check of the feature that $\partial u_i/\partial x_j$ is accurate if integrated along particle trajectories can be made by looking at the conservation of divergence of the material field $\boldsymbol{l}$, determined by the matrix $\boldsymbol{B}$ which in turn is defined by the matrix $\partial u_i/\partial x_j$.

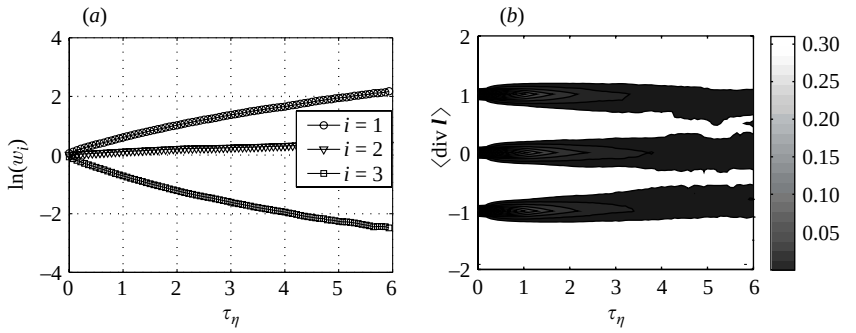

FIGURE 7. (*a*) The evolution in time of the mean eigenvalues, $\langle w_i \rangle$, of the Gauchy–Green tensor, $\boldsymbol{W}$, is shown. (*b*) PDFs of three different sets of div $\boldsymbol{l}$ which had initial values of $-1, 0$ and 1. Only after a few τ_η the peaks are shifted slightly towards their random distribution, which is centred around zero.

The expression

$$\frac{\mathrm{D}\boldsymbol{l}}{\mathrm{D}t} = (\boldsymbol{l} \cdot \nabla)\boldsymbol{u} \tag{31}$$

can be written as

$$\frac{\partial \boldsymbol{l}}{\partial t} = \mathrm{rot}(\boldsymbol{u} \times \boldsymbol{l}) - \boldsymbol{u}\,\mathrm{div}\,\boldsymbol{l}. \tag{32}$$

Taking the div of this equation, we find that for any material field, $\boldsymbol{l}$

$$\frac{\mathrm{D}(\mathrm{div}\,\boldsymbol{l})}{\mathrm{D}t} = 0, \tag{33}$$

which means that div $\boldsymbol{l}$ is a pointwise Lagrangian invariant. This is important since no diffusivity is involved here. Three initial sets of div $\boldsymbol{l} = -1, 0, 1$ were created randomly and then the evolution of their initial values was monitored along their trajectories, as shown in figure 7(*b*). Up to a time of $6\,\tau_\eta$ the initial values of div $\boldsymbol{l}$ are conserved within 20% of the initial separation of the three sets.

The above checks thus show that spatial velocity derivatives can be obtained at reasonable accuracy by applying the procedures presented here to the 3D-PTV measurements. The use of weighted polynomials which are fitted along particle trajectories using, preferably, information form points with low relative divergence always results in improved accuracy for temporal and spatial velocity derivatives. Relative divergence, $\delta < 0.1$, used as a criterion to select data for a statistical set has been shown to work satisfactorily.

2.4.2. *Representativeness*

It is desirable to demonstrate that there is no bias in the 'surviving' data set. The question to be asked is: do the derived velocity derivatives represent only a subset of the flow that is comprised of weak events, e.g. does the method work well for slow and low-accelerated flow regions with a low level of dissipation only? In figure 8 we show that this is not the case. For trajectory points where relative divergence, δ, is below 0.1 the PDFs of kinetic energy, $\boldsymbol{u}^2$ and $\boldsymbol{a}^2$ perfectly match those for the entire data set (figure 8*a*, *b*). Also the second-order longitudinal and transversal structure functions $\langle \delta v_\parallel^2(r) \rangle$, $\langle \delta v_\perp^2(r) \rangle$ as well as $\langle \Delta \boldsymbol{u}(r) \cdot \Delta \boldsymbol{a}(r) \rangle$, which are all associated more directly with velocity derivatives, again show no significant systematic differences between the sets with $\delta < 0.1$ and the entire set (figure 8*c*, *d*). Even the differences that can actually

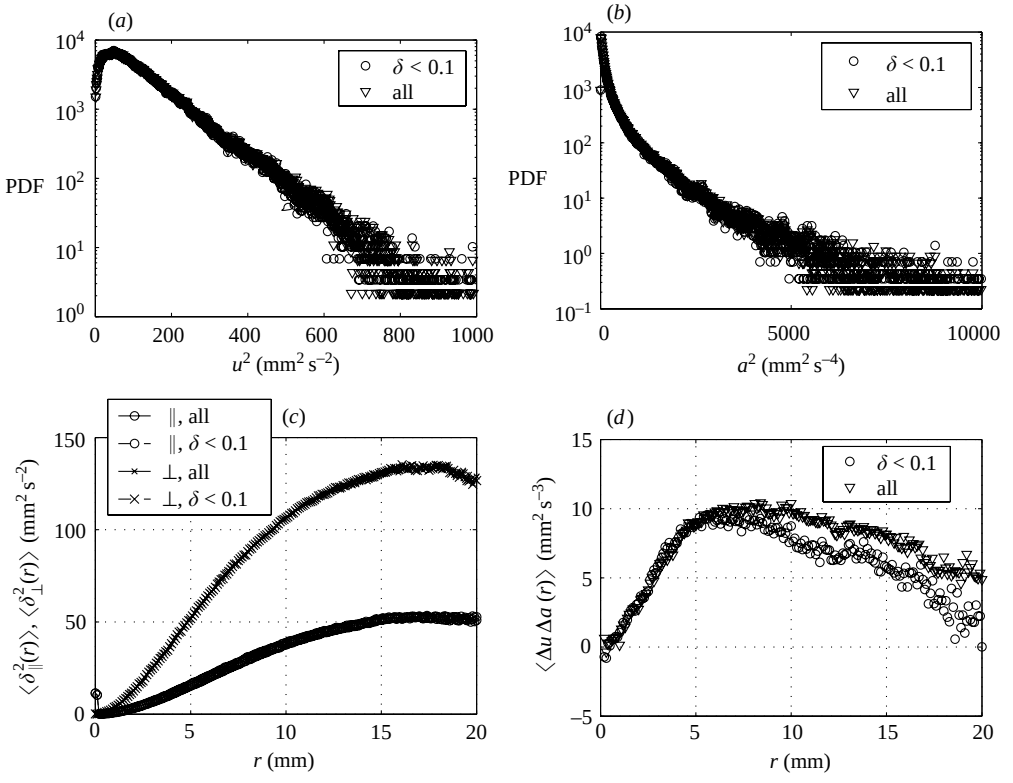

FIGURE 8. PDFs of data restricted to $\delta < 0.1$ and the entire set for (a) kinetic energy, $u_i u_i$, (b) energy of Lagrangian acceleration, $a_i a_i$, (c) longitudinal and transversal second-order structure function, (d) the structure function, $\Delta \boldsymbol{u} \cdot \Delta \boldsymbol{a}$.

be seen in figure (8d) at $r > 10\,\mathrm{mm}$ of $O(2\,\mathrm{mm^2\,s^{-3}})$ are small if compared to the large values the scalar product $\Delta \boldsymbol{u}(\boldsymbol{r}) \cdot \Delta \boldsymbol{a}(\boldsymbol{r})$, $\boldsymbol{r} > 10\,\mathrm{mm}$, can take with rms for $\Delta \boldsymbol{u}$ and $\Delta \boldsymbol{a}$ of $O(10\,\mathrm{mm\,s^{-1}})$ and $O(10\,\mathrm{mm\,s^{-2}})$. The velocity difference is

$$\delta v(\boldsymbol{r}) \equiv \boldsymbol{u}(\boldsymbol{x} + \boldsymbol{r}) - \boldsymbol{u}(\boldsymbol{x}) \tag{34}$$

with $\delta v_\parallel$ the component of δv that is parallel to $\boldsymbol{r}$, and $\delta v_\perp$ the component perpendicular to $\boldsymbol{r}$. $\langle \cdot \rangle$ here denotes averaging over all $\boldsymbol{r}$ with $\|\boldsymbol{r}\| = r$. Similarly, for $\langle \Delta \boldsymbol{u}(r) \cdot \Delta \boldsymbol{a}(r) \rangle$ we have

$$\Delta \boldsymbol{u}(\boldsymbol{r}) \cdot \Delta \boldsymbol{a}(\boldsymbol{r}) \equiv [\boldsymbol{u}(\boldsymbol{x} + \boldsymbol{r}) - \boldsymbol{u}(\boldsymbol{x})] \cdot [\boldsymbol{a}(\boldsymbol{x} + \boldsymbol{r}) - \boldsymbol{a}(\boldsymbol{x})] \tag{35}$$

and $\langle \cdot \rangle$ again denotes averaging over all $\boldsymbol{r}$ with $\|\boldsymbol{r}\| = r$.

3. Eulerian results

The novelty of the results presented is that they comprise the first successful non-intrusive turbulent flow measurements of the full set of spatial and temporal velocity derivatives, not only for a fixed point in space but also along fluid particle trajectories. In a first step, selected Eulerian results on geometrical statistics of vorticity and on strain demonstrate the capability of 3D-PTV to recover most of the relevant results on the turbulent fine-scale structure which have been obtained until now from DNS and

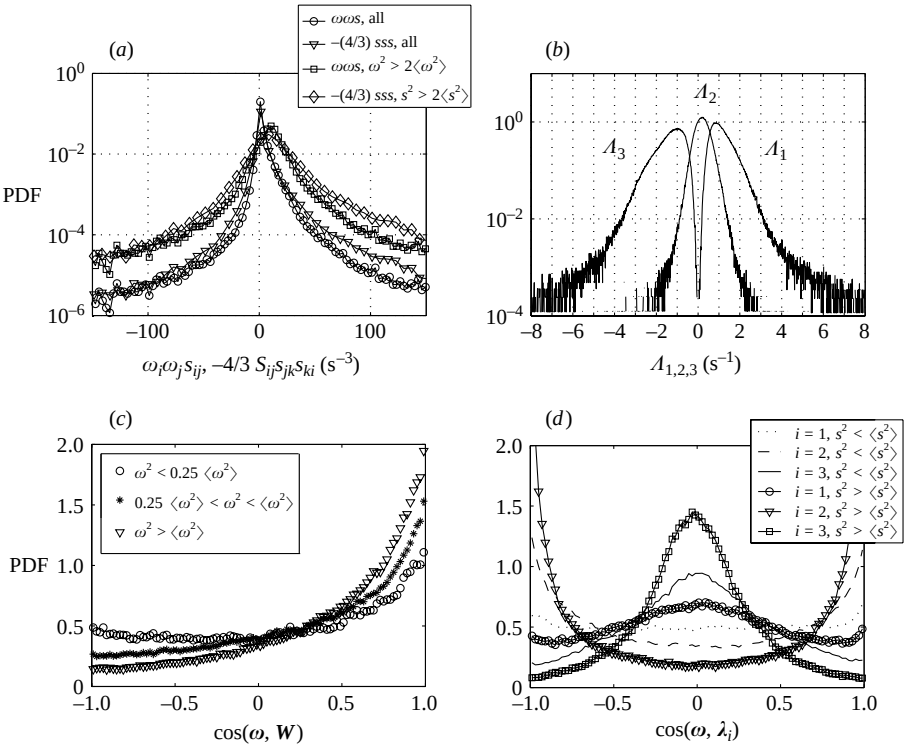

FIGURE 9. (*a*) PDFs of $\omega_i\omega_j s_{ij}$ and $-\frac{4}{3}s_{ij}s_{jk}s_{ki}$ conditioned on high strain or high enstrophy. (*b*) PDFs of the eigenvalues, $\Lambda_{1,2,3}$, of the rate of strain tensor s_{ij}. (*c*) PDFs of $\cos(\boldsymbol{\omega}, \boldsymbol{W})$ conditioned on ω^2. (*d*) PDFs of $\cos(\boldsymbol{\omega}, \boldsymbol{\lambda}_i)$ conditioned on weak and strong s^2.

hot-wire experiments only (Betchov 1956; Tsinober *et al.* 1992; Kholmyansky *et al.* 2001). This sets the stage for the following section, § 4, on Lagrangian results. The selection reproduces features of turbulence most of which are not observed in a Gaussian flow field, i.e. are specific to genuine fluid turbulence (Shtilman, Spector & Tsinober 1993). They obtained a number of rigorous results on random Gaussian solenoidal velocity fields. Some of these results directly concern properties of vorticity and strain.

In particular, it was shown that the PDFs of enstrophy production $\omega_i\omega_j s_{ij}$ and production of strain $-s_{ij}s_{jk}s_{ki}$ are strictly symmetric for a random Gaussian velocity field. In that way the production terms comprise the most basic difference to a turbulent velocity field. In figure 9(*a*) the PDFs of $\omega_i\omega_j s_{ij}$ and $-\frac{4}{3}s_{ij}s_{jk}s_{ki}$ show how both enstrophy and strain production are positively skewed for a turbulent flow. In addition we note that if $\omega_i\omega_j s_{ij}$ is conditioned on high $\boldsymbol{\omega}^2$ or $-\frac{4}{3}s_{ij}s_{jk}s_{ki}$ is conditioned on high s^2 the PDFs – while remaining positively skewed – become flatter, favouring higher probabilities of strong production or destruction events and that the peaks of the most probable events themselves are shifted towards the positive regime.

In figure 9(*b*) the PDFs of the eigenvalues $\Lambda_{1,2,3}$ of the rate of strain tensor, s_{ij}, are given. The main feature is the positively skewed PDF of Λ_2 which is a fundamental property of turbulence (Tsinober *et al.* 1997). Again in a Gaussian velocity field this feature is non-existent and $\langle\Lambda_2\rangle = 0$. It is essentially responsible for 'everything' since without it, turbulence would not be able to produce strain and therefore no enstrophy.

$\langle \omega^2 \Lambda_1 \cos^2(\omega, \lambda_1)\rangle$	$\langle \omega^2 \Lambda_2 \cos^2(\omega, \lambda_2)\rangle$	$\langle \omega^2 \Lambda_3 \cos^2(\omega, \lambda_3)\rangle$
$1.79\,\mathrm{s}^{-3}$	$0.50\,\mathrm{s}^{-3}$	$-1.29\,\mathrm{s}^{-3}$
$\langle \omega^2 \Lambda_1^2 \cos^2(\omega, \lambda_1)\rangle$	$\langle \omega^2 \Lambda_2^2 \cos^2(\omega, \lambda_2)\rangle$	$\langle \omega^2 \Lambda_3^2 \cos^2(\omega, \lambda_3)\rangle$
$0.50\,\mathrm{s}^{-4}$	$0.11\,\mathrm{s}^{-4}$	$0.39\,\mathrm{s}^{-4}$

TABLE 3. Contributions of terms associated with Λ_i to mean enstrophy production, $\langle \omega_i \omega_j s_{ij}\rangle$, and to the magnitude of the vortex stretching vector, W^2.

The strain production term, $-s_{ij}s_{jk}s_{ki}$, of expression (2) is equivalent to $-\Lambda_1\Lambda_2\Lambda_3$. $\langle -\Lambda_1\Lambda_2\Lambda_3\rangle$ would be identically zero for a symmetrically distributed Λ_2 as e.g. for a Gaussian velocity field. The magnitude of $\langle \Lambda_2\rangle \approx 0.2\,\mathrm{s}^{-1}$ remains relatively small compared to $\langle \Lambda_1\rangle \approx 1\,\mathrm{s}^{-1}$ and $\langle \Lambda_3\rangle \approx -1.2\,\mathrm{s}^{-1}$. The ratio of $\langle \Lambda_1\rangle : \langle \Lambda_2\rangle : \langle \Lambda_3\rangle$ is consistent with findings from numerical simulations reported in e.g. Girimaji & Pope (1990), Dresselhaus & Tabor (1994), Huang (1996) and Tsinober (2001) and hot-wire experiments (Kholmyansky *et al.* 2001).

A strong manifestation of the positiveness of mean enstrophy production is shown through the PDFs of $\cos(\boldsymbol{\omega}, \boldsymbol{W})$ in figure 9(*c*). The physical interpretation of the geometrical invariant $\cos(\boldsymbol{\omega}, \boldsymbol{W})$ is straightforward. It is positive when the projection of the vortex stretching vector, $\boldsymbol{W}$, on $\boldsymbol{\omega}$ points in the same direction as vorticity and thus vortex stretching occurs. If $\cos(\boldsymbol{\omega}, \boldsymbol{W})$ is zero it will only attempt to tilt the direction of $\boldsymbol{\omega}$ and if it is negative then vorticity is compressed. It could be argued that the positively skewed cosine alone does not prove the positiveness of $\langle \omega_i \omega_j s_{ij}\rangle$ since the magnitude of $\boldsymbol{\omega}$ could be anti-correlated with $\cos(\boldsymbol{\omega}, \boldsymbol{W})$ resulting in a net vortex compression. However, conditioning $\cos(\boldsymbol{\omega}, \boldsymbol{W})$ on $\boldsymbol{\omega}^2$ reveals that the contrary is the case: stronger $\boldsymbol{\omega}^2$ events are correlated with stronger positive skewness of $\cos(\boldsymbol{\omega}, \boldsymbol{W})$. The PDF of $\cos(\boldsymbol{\omega}, \boldsymbol{W})$ for a Gaussian velocity field is a symmetric curve centred around zero (Shtilman *et al.* 1993).

One of the best known manifestations of turbulence having a dynamically relevant structure even in low-intensity regions is the orientation of $\boldsymbol{\omega}$ relative to the eigenframe of the rate of strain tensor s_{ij}, $\cos(\boldsymbol{\omega}, \boldsymbol{\lambda}_i)$. Figure 9(*d*) shows the PDFs of $\cos(\boldsymbol{\omega}, \boldsymbol{\lambda}_i)$ conditioned on weak and strong strain. The main feature is the predominant alignment of $\boldsymbol{\omega}$ with the intermediate eigenvector $\boldsymbol{\lambda}_2$ of the rate of strain tensor, a feature recognized by Siggia (1981), first reported by Ashurst *et al.* (1987) and confirmed in Tsinober *et al.* (1992) and references therein. The preferential alignments increase with higher strain and even for weak events the preferential alignments persist, suggesting that turbulence also has structure in less intense regimes. Again, in a random field the PDFs of $\cos(\boldsymbol{\omega}, \boldsymbol{\lambda}_i)$ are precisely flat.

The combined effect of the alignment between $\boldsymbol{\omega}$ and $\boldsymbol{\lambda}_i$ and the behaviour of Λ_i leads to unusual contributions to the mean magnitude of the vortex stretching vector, W^2, and the mean enstrophy production $\langle \omega_i \omega_j s_{ij}\rangle$ from the three terms associated with each Λ_i, $W^2 = \boldsymbol{\omega}^2 \Lambda_i^2 \cos^2(\boldsymbol{\omega}, \boldsymbol{\lambda}_i)$ and $\omega_i \omega_j s_{ij} = \boldsymbol{\omega}^2 \Lambda_i \cos^2(\boldsymbol{\omega}, \boldsymbol{\lambda}_i)$, which are given in table 3. Since the magnitude of Λ_2 is much smaller than the magnitude of Λ_1, and Λ_2 takes both positive and negative values (figure 9*b*), the largest contribution to $\langle \omega_i \omega_j s_{ij}\rangle$ is associated with the first term, Λ_1, despite the preferential alignment between $\boldsymbol{\omega}$ and $\boldsymbol{\lambda}_2$, as is explained by Kholmyansky *et al.* (2001). Similarly the largest contribution to vortex stretching $\langle \boldsymbol{W}^2\rangle$ comes also from the term associated with Λ_1.

4. Lagrangian results

4.1. *Material lines*

Infinitesimal material lines, $\boldsymbol{l}$, are studied following the work of Batchelor (1952), Monin & Yaglom (1997) and Girimaji & Pope (1990). Study of the evolution of material elements is important in a variety of contexts, e.g. because they are directly related to the diffusive characteristics of turbulence and evolution of passive vectors in random flows (kinematic dynamos). Here however, our interest in the study of material lines is motivated by their relevance in the context of vortex stretching or enstrophy growth control. The commonly held view that vortex stretching is due to material line stretching has been proved too simple since it is known that (i) material line stretching is stronger than vortex stretching and (ii) material lines have a strong tendency to align with the most positive principal axis of strain while vorticity tends to align with the intermediate principal axis (Girimaji & Pope 1990; Dresselhaus & Tabor 1994; Huang 1996). A detailed list of differences between material lines and vortex lines is given in Tsinober (2001) and important additions are found in Tsinober & Galanti (2003). After demonstrating that we find the same results with the experiment presented here, and thus proving the capability of 3D-PTV to follow material lines for some τ_η, we focus our attention on special material elements, $\boldsymbol{l}_0$, which at some time τ_0 are perfectly aligned with vorticity ($\boldsymbol{l}_0 = \omega_0$). This contributes to the understanding of why vorticity tends to align with the intermediate principal axis and thus experiences a significantly moderated growth rate. Is this only due to viscosity? To what degree is it due to the nonlinear interaction of vorticity with its surrounding flow?

The mean rates at which material lines are being stretched, $\langle l_i l_j s_{ij}/l^2 \rangle$, have been studied since 1949 (Batchelor & Townsend 1949; Batchelor 1952; Girimaji & Pope 1990; Dresselhaus & Tabor 1994; Huang 1996). From these studies it is known that $\langle l_i l_j s_{ij}/l^2 \rangle$ is larger than the intermediate principal rate, Λ_2, but smaller than the most positive one, Λ_1. It is also known that the mean stretching rates of material lines are larger than the mean stretching rates of vorticity, $\langle \omega_i \omega_j s_{ij}/\omega^2 \rangle$. These results are reproduced with our 3D-PTV measurements and summarized in figure 10(*a*).

From the assumption of persistent straining it follows directly that $\boldsymbol{l}$ should align with the most positive principal axis of strain (Batchelor 1952). Figures 10(*b–d*) show the evolution in time of the PDFs of $\cos(\boldsymbol{l}, \boldsymbol{\lambda}_1)$, $\cos(\boldsymbol{l}, \boldsymbol{\lambda}_2)$ and $\cos(\boldsymbol{l}, \boldsymbol{\lambda}_3)$. A clear but non-perfect alignment of $\boldsymbol{l}$ with $\boldsymbol{\lambda}_1$ can be observed after a transition time of $2\tau_\eta$, the PDFs for $\cos(\boldsymbol{l}, \boldsymbol{\lambda}_2)$ reveal a flat distribution for all times, and the PDFs for $\cos(\boldsymbol{l}, \boldsymbol{\lambda}_3)$ show that $\boldsymbol{l}$ is predominantly oriented perpendicular to $\boldsymbol{\lambda}_3$. Two papers deal mainly with the issue of persistency of straining of material lines. Girimaji & Pope (1990) attribute the smaller than expected stretching rates and $\cos(\boldsymbol{l}, \boldsymbol{\lambda}_1)$ to the effects of vorticity and 'non-persistent straining'. They conclude that the misaligning effects are due to the rotation of the principal strain axes. Dresselhaus & Tabor (1994) point out that it is obvious that vorticity and strain rotation are dynamically dependent and derive expressions that identify the role played by the competing effects of vorticity and strain-basis rotation. However, they arrive at the conjecture that vortex line stretching should be greater than material line stretching, which is confirmed neither by DNS (Huang 1996) nor by our experiment.

In the context of growth control of enstrophy we now look at material elements, $\boldsymbol{l}_0$, which at some time τ_0 are perfectly aligned with vorticity ($\boldsymbol{l}_0 = \boldsymbol{\omega}_0$). Tsinober & Galanti (2001, 2003) and Ohkitani (2002) report that passive vectors align with $\boldsymbol{\lambda}_2$ when a diffusive term for material elements $\boldsymbol{l}$ is added to the transport equation (4)

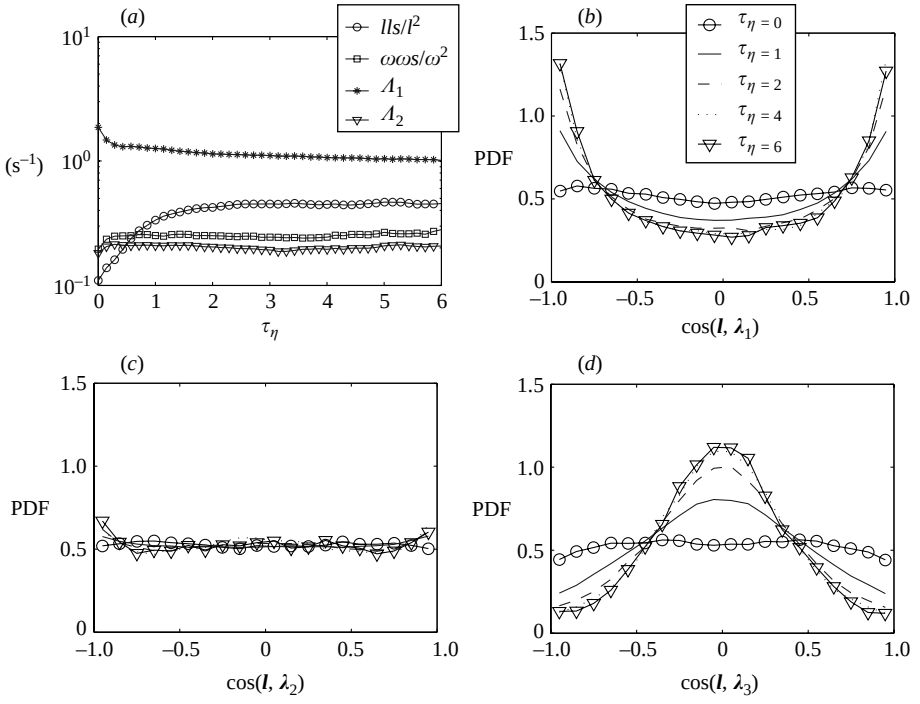

FIGURE 10. (*a*) Mean stretching rates of material lines, $\langle l_i l_j s_{ij}/l^2 \rangle$, mean stretching rates of vortex lines, $\langle \omega_i \omega_j s_{ij}/\omega^2 \rangle$, and means of the intermediate (∇—) and most positive (*—) principal strain rate, $\langle \Lambda_2 \rangle$ and $\langle \Lambda_1 \rangle$ plotted over time. (*b*–*d*) PDFs of $\cos(l, \lambda_{1,2,3})$ for randomly selected l for different times.

as

$$\mathrm{D}l_i/\mathrm{D}t = l_j \partial u_i/\partial x_j + \nu \nabla^2 l_i. \tag{36}$$

From this, the conclusion could be drawn that only the viscous term is responsible for any vector, vorticity or material line, aligning with $\boldsymbol{\lambda}_2$. However, from figure 11 we learn that the matter is more complicated.

In figure 11(*a*) the evolution of the PDFs of $\cos(\boldsymbol{l}, \boldsymbol{W}^l)$ for material elements with $\boldsymbol{l}_0 = \boldsymbol{\omega}_0$ is shown. Over a time interval of $\tau_\eta = 0$–6 only a slight reduction of the material line compression and a slight increase of the material line stretching events can be observed while the skewness essentially remains low. Figure 11(*b*) shows the evolution in time of the PDFs of $\cos(\boldsymbol{l}, \lambda_2)$, with $\boldsymbol{l}_0 = \boldsymbol{\omega}_0$. Again, the evolution is not quite as expected since we observe that at relatively late times, $\tau_\eta = 6$, a significant alignment of $\boldsymbol{l}$ with $\boldsymbol{\lambda}_2$ still persists. Contrary to the experience that events associated with material lines require a transition time of no more than $\tau_\eta = 2$, as is the case for random $\boldsymbol{l}$ until they reach their stable stretching rate and until they reach their stable alignment with $\boldsymbol{\lambda}_1$, we note that line elements with $\boldsymbol{l}_0 = \boldsymbol{\omega}_0$ are much more reluctant to act as we would expect them to. It is a clear indication that the nonlinear interaction of vorticity with strain influences the vicinity of the fluid that surrounds vortex lines – and hence also special material lines – in a way that $\boldsymbol{\lambda}_2$ alignments can persist. Two explanations are possible. Either the interaction is directly stabilizing $\boldsymbol{\lambda}_2$ alignments for passive vectors also, or the interaction is simply stabilizing $\boldsymbol{\omega}$ alignment of $\boldsymbol{l}$, which will also result in persistent $\boldsymbol{\lambda}_2$ alignment. In figure 11(*c*) $\langle \cos(\boldsymbol{l}, \boldsymbol{\lambda}_2) \rangle$ with $\boldsymbol{l}_0 = \boldsymbol{\omega}_0$ is conditioned on weak and strong strain and weak and strong enstrophy

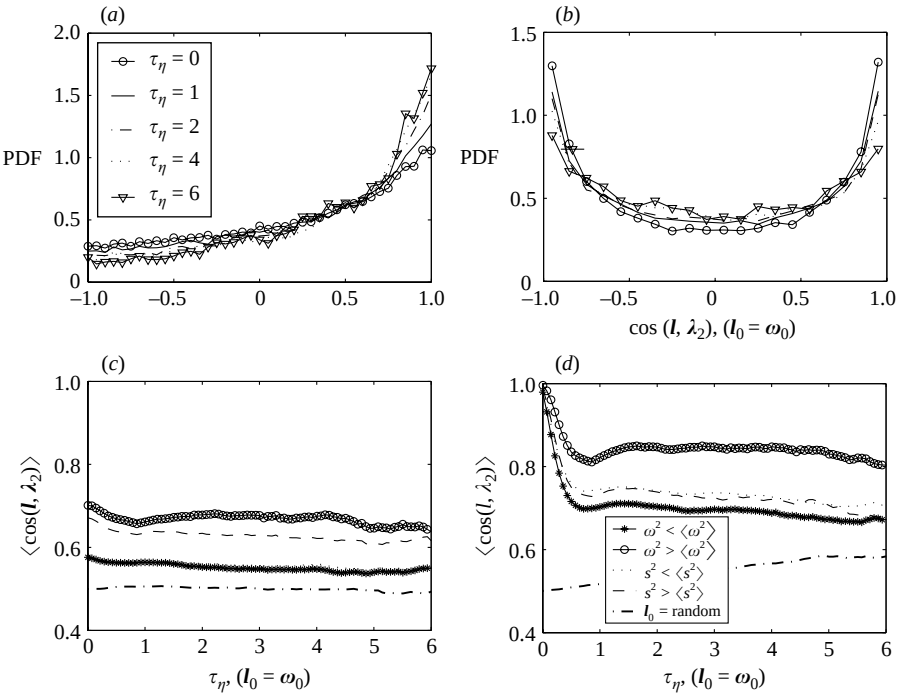

FIGURE 11. (*a*) $\cos(\boldsymbol{l}, W^l)$ with $\boldsymbol{l}_0 = \boldsymbol{\omega}_0$, for $\tau_\eta = 0$–6. (*b*) Evolution in time of the PDFs of $\cos(\boldsymbol{l}, \boldsymbol{\lambda}_2)$ with $\boldsymbol{l}_0 = \boldsymbol{\omega}_0$, for $\tau_\eta = 0$–6. (*c*) Mean $\cos(\boldsymbol{l}, \boldsymbol{\lambda}_2)$ for $\boldsymbol{l}_0 = \boldsymbol{\omega}_0$ and (*d*) mean $\cos(\boldsymbol{l}, \boldsymbol{\omega})$ plotted over time for $\tau_\eta = 0$–6 conditioned on low and high strain and enstrophy.

and plotted over time. $\langle \cos(\boldsymbol{l}, \boldsymbol{\lambda}_2) \rangle$ is found to be higher for elements conditioned on strong enstrophy than for elements conditioned on strong strain. This suggests that the interaction is driven more by enstrophy than by strain. In figure 11(*d*) the evolution of $\langle \cos(\boldsymbol{l}, \boldsymbol{\omega}) \rangle$ is conditioned on the strength of strain and enstrophy events. We observe that here the magnitude of vorticity solely determines how much nonlinear interaction occurs in order to keep $\boldsymbol{l}$ aligned with $\boldsymbol{\omega}$. After a sharp initial decay in the first τ_η we observe a constant value of $\langle \cos(\boldsymbol{l}, \boldsymbol{\omega}) \rangle \sim 0.8$ for strong enstrophy which is significantly higher than the corresponding value for $\langle \cos(\boldsymbol{l}, \boldsymbol{\lambda}_2) \rangle \sim 0.6$.

The results in figure 11(*d*) suggest that, probably more than anything else, material lines keep their $\boldsymbol{\lambda}_2$-orientation due to the fact that they are effectively hijacked by vorticity. If we recall that the evolution of $\boldsymbol{l}$ is determined by the evolution of $\boldsymbol{B}$, then the above result on the persistently high $\langle \cos(\boldsymbol{l}, \boldsymbol{\omega}) \rangle$ implies that when tilting of $\boldsymbol{l}$ with respect to $\boldsymbol{\omega}$ is suppressed, then also the rotation of the tensor $\partial u_i / \partial x_j$ – which defines $\boldsymbol{l}$ through $\boldsymbol{B}$ (expression (29)) – with respect to $\boldsymbol{\omega}$ is suppressed! We can thus speculate that the component of $\partial u_i / \partial x_j$, the eigenframe of strain, $\boldsymbol{\lambda}_i$, also experiences a suppressed tilting with respect to $\boldsymbol{\omega}$. Strong enstrophy and its interaction with the surrounding flow may therefore be capable of stabilizing an already existing $\boldsymbol{\lambda}_2$ alignment. The vorticity–flow interaction effect, however, only assists the effect of the viscous term $\upsilon \nabla^2 \omega_i$. This term is responsible for the diffusive vectors following the strain basis orientation to establish a $\boldsymbol{\lambda}_2$ alignment. This is consistent with the fact that $\boldsymbol{\lambda}_2$ alignment is most pronounced in strong events where $\upsilon \nabla^2 \omega_i$ can also be expected to be strong.

We find that whenever the field of velocity derivatives is intensive the fine-scale structure of turbulence is such that it creates and maintains vorticity orientations that

$\frac{1}{2}(\mathrm{D}\omega^2/\mathrm{D}t)$	$\omega_i\omega_j s_{ij}$	$\nu\omega_i\nabla^2\omega$	$\frac{1}{2}(\mathrm{D}l^2/\mathrm{D}t)$	$l_i l_j s_{ij}$
36%	32%	48%	13%	37%

TABLE 4. Relative errors of enstrophy and material line budget terms, based on their r.m.s. values.

are preferentially $\boldsymbol{\lambda}_2$-aligned. The consequences are that preferentially when the field of velocity derivatives would be ideal for strong production of vorticity, $\boldsymbol{\omega}^2$-growth is moderated through a strong $\boldsymbol{\lambda}_2$-alignment. Assisted by viscosity and the vorticity–flow interaction, enstrophy exhibits a nonlinear saturation, resulting in contributions to $\omega_i\omega_j s_{ij}$ that are associated with the weaker term $\boldsymbol{\omega}^2\Lambda_2\cos^2(\boldsymbol{\omega},\boldsymbol{\lambda}_2)$ rather than with $\boldsymbol{\omega}^2\Lambda_1\cos^2(\boldsymbol{\omega},\boldsymbol{\lambda}_1)$. In other words vorticity, in order to control its growth, has not only a self-amplification mechanism but it also has a self-moderating mechanism which is associated with nonlinear saturation and action of viscosity.

4.2. *Viscous change of enstrophy*

For a flow with a statistically stationary level of enstrophy it is clear that mean enstrophy production has to be balanced by its viscous destruction as (Taylor 1938)

$$\langle\omega_i\omega_j s_{ij}\rangle = -\langle\nu\omega_i\nabla^2\omega_i\rangle. \tag{37}$$

It has been reported by Tsinober (2001) that the overall enstrophy production and its viscous destruction integrated over the entire domain are also approximately balanced at any moment in time, i.e.

$$\frac{\mathrm{D}\left(\frac{1}{V}\int\omega^2\,\mathrm{d}V\right)}{\mathrm{D}t} \ll \frac{1}{V}\int\omega_i\omega_j s_{ij}\,\mathrm{d}V \sim -\frac{\nu}{V}\int\omega_i\nabla^2\omega_i\,\mathrm{d}V. \tag{38}$$

From a DNS box turbulence simulation at $Re_\lambda = 75$ it is further reported that in a wide range of enstrophy events, up to $\omega^2/\langle\omega^2\rangle = 4$, the mean production due to vortex stretching is approximately balanced by mean viscous destruction not only over an entire domain at any moment but also if conditioned on the magnitude of vorticity (Tsinober 2001) as

$$\langle\omega_i\omega_j s_{ij}\ |_{\omega^2}\rangle \approx -\langle\nu\omega_i\nabla^2\omega_i\ |_{\omega^2}\rangle. \tag{39}$$

For high strain events, $s^2/\langle s^2\rangle > 2$, enstrophy production is reported to become considerably larger than its viscous destruction as

$$\langle\omega_i\omega_j s_{ij}\ |_{s^2}\rangle \gg -\langle\nu\omega_i\nabla^2\omega_i\ |_{s^2}\rangle. \tag{40}$$

These findings raise the question of if and how that equilibrium is reflected in the pointwise relations between the terms making up the enstrophy budget of expression (1).

With our method we can directly measure $\omega_i\omega_j s_{ij}$ and $\frac{1}{2}(\mathrm{D}\boldsymbol{\omega}^2/\mathrm{D}t)$ but the viscous term, $\nu\omega_i\nabla^2\omega_i$, has to be taken as the difference of the two measured terms. The good agreement between the theoretically predicted and measured error in the above section for checks on divergence, acceleration and material line evolution justifies an attempt also to estimate the accuracy for the higher-order terms of the enstrophy budget. Following the same approach we arrive at the result that the r.m.s.-based relative accuracy of these terms is 30–40 %. The results are summarized in table 4 and their derivation is outlined in Appendix A. A verification is possible via the

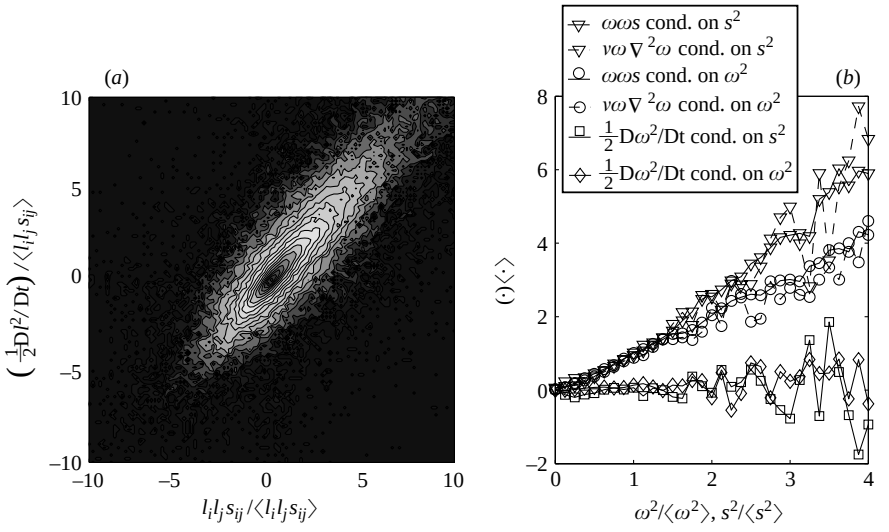

FIGURE 12. (*a*) Joint PDF of $\frac{1}{2}(\mathrm{D}l^2/\mathrm{D}t)$ versus $l_i l_j s_{ij}$ normalized by $\langle l_i l_j s_{ij}\rangle$, with $\boldsymbol{l}$ comprised by two measured particles, separated no more than 3.5 mm. (*b*) Normalized means of the three enstrophy transport equation terms conditioned on strain and enstrophy.

corresponding terms for material line evolution. For $\frac{1}{2}(\mathrm{D}l^2/\mathrm{D}t)$ and $l_i l_j s_{ij}$ we have both a theoretical prediction for the r.m.s.-based relative errors, 13% and 37%, and a simple check – a joint PDF of $\frac{1}{2}(\mathrm{D}l^2/\mathrm{D}t)$ versus $l_i l_j s_{ij}$. From the error prediction we can expect such a joint PDF to have elliptical contour shapes with their main axis parallel to the diagonal and with aspect ratios $1/n$ as

$$n = \min\left[\left(\varepsilon_{\frac{1}{2}\mathrm{D}l^2/\mathrm{D}t}\right)^{-1}, \left(\varepsilon_{lls}\right)^{-1}\right] = 2.7. \tag{41}$$

From figure 12(*a*) an aspect ratio, $1/n$, of 1/3 can be measured. The good agreement of theoretical and measured values thus supports the above approach, and also for the prediction of the errors $\varepsilon_{\frac{1}{2}\mathrm{D}\omega^2/\mathrm{D}t}$, $\varepsilon_{\omega\omega s}$, and $\varepsilon_{\nu\omega\nabla^2\omega}$ of the enstrophy budget terms. Further we see from figure 12(*a*) that despite the fact that the difference in accuracy for $\frac{1}{2}(\mathrm{D}l^2/\mathrm{D}t)$ and $l_i l_j s_{ij}$, being 13% and 37%, is considerable, this is not reflected in large systematic errors such as strong off-diagonal contours. As an additional verification we show in figure 12(*b*) that there is good qualitative agreement with the DNS results mentioned above in the sense that the approximate balance of production of enstrophy and its viscous destruction is recovered for intensities of enstrophy of up to $\omega^2/\langle\omega^2\rangle \approx 4$. Further, we also find higher vortex production in regions with strong strain rather than strong enstrophy. Contrary to the DNS results we find that for high strain events production and viscous destruction of enstrophy is also balanced. This may be explained in part by the reduced observability of strong strain events, leading to under-resolution of the field of velocity derivatives in our experiments. The balance is reflected in the conditional means for $\frac{1}{2}(\mathrm{D}\boldsymbol{\omega}^2/\mathrm{D}t)$ which are found to be close to zero, i.e. the level of vorticity associated with regions of different strengths of strain or enstrophy is more or less constant.

We now look at the joint PDF of $\omega_i\omega_j s_{ij}$ versus $\frac{1}{2}(\mathrm{D}\boldsymbol{\omega}^2/\mathrm{D}t)$ shown in figure 13(*a*). The main feature is that there is no pointwise relation between production of enstrophy and actual change of enstrophy, even though it appears that positive

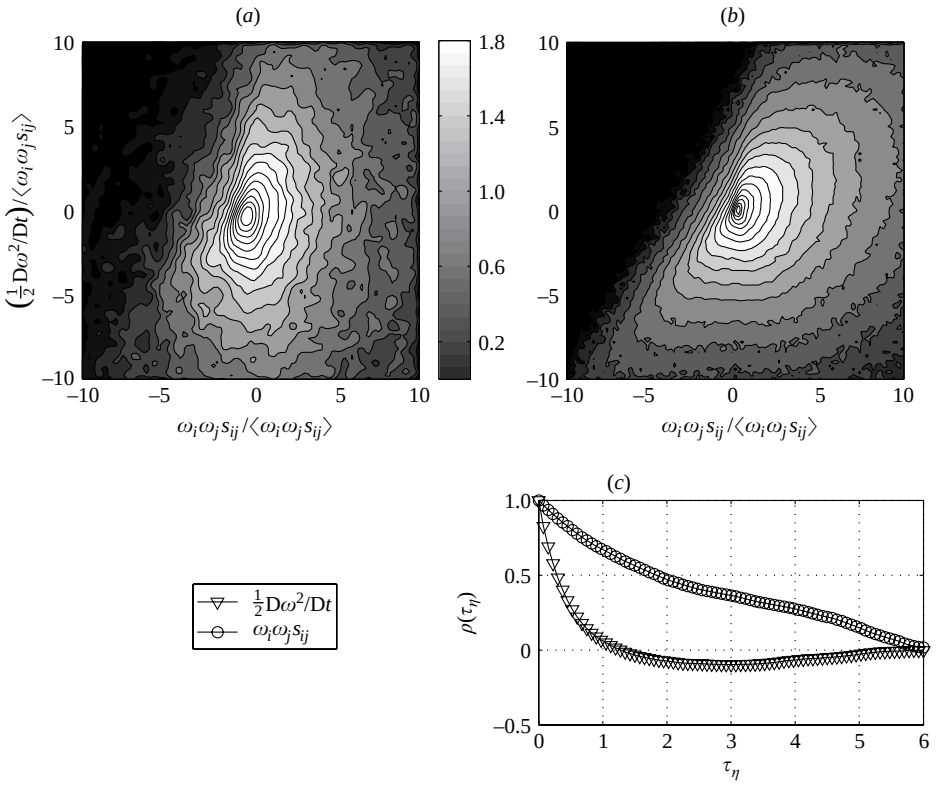

FIGURE 13. Joint PDF plot of vorticity production versus change of enstrophy, both axes normalized with $\langle\omega_i\omega_j s_{ij}\rangle$: (*a*) as obtained from a PTV experiment and (*b*) as obtained from 256^3 DNS. (*c*) Lagrangian auto correlation coefficients of two enstrophy budget terms.

enstrophy changes are mostly associated with positive enstrophy production events. We also note that the term $\frac{1}{2}(D\boldsymbol{\omega}^2/Dt)$ takes significantly larger instantaneous values than $\omega_i\omega_j s_{ij}$. In view of the balancing reflected in expression (38) this is somewhat counter-intuitive, as it appears that the interaction of strain and vorticity through $\omega_i\omega_j s_{ij}$ is nowhere close even to being pointwise balanced by $\nu\omega_i\nabla^2\omega_i$, i.e. overall balancing of $\omega_i\omega_j s_{ij}$ and $\nu\omega_i\nabla^2\omega_i$ appears to be a non-local process. The experimental results shown in figure 13(*a*) are similar to those obtained for a 256^3 DNS simulation of forced Navier–Stokes equations in a cubic box with periodic boundary conditions at $Re_\lambda \approx 100$ (Galanti & Tsinober 2004) that are shown in 13(*b*). Also here, positive enstrophy changes are mostly to be observed along with positive enstrophy production events. Just as for the experimental results in figure 13(*a*) a positive value for $\omega_i\omega_j s_{ij}$ is not strongly correlated with positive $\frac{1}{2}(D\boldsymbol{\omega}^2/Dt)$ events and for the DNS results the term $\frac{1}{2}(D\boldsymbol{\omega}^2/Dt)$ also takes larger instantaneous values than the term $\omega_i\omega_j s_{ij}$.

One important implication of the observed behaviour is that the only term left that could be responsible for the strong $\frac{1}{2}(D\boldsymbol{\omega}^2/Dt)$ events is the viscous term, $\nu\omega_i\nabla^2\omega_i$. How can it be that $\omega_i\omega_j s_{ij}$ and $\nu\omega_i\nabla^2\omega_i$ integrated over a domain are reported to be balanced at any moment, but that at the same time the two terms exhibit such a different behaviour, resulting in large instantaneous values for $\frac{1}{2}(D\boldsymbol{\omega}^2/Dt)$? A possible explanation could be that the viscous term is associated with faster processes compared to the much slower interaction of strain and vorticity, as we will see

below. This would explain the pointwise imbalance. At the same time however, the viscous term may fluctuate around a moving mean value of $-\omega_i\omega_j s_{ij}$ and thereby neutralize the work of $\omega_i\omega_j s_{ij}$ towards a net enstrophy production. This will result in a balanced enstrophy production – not pointwise, but in a Lagrangian sense, i.e. averaged over a few time scales along a particle trajectory enstrophy change will be only small. Support for this scenario is given in figure 13(*c*) where the Lagrangian auto-correlation coefficients for two enstrophy budget terms are given. The enstrophy production, $\omega_i\omega_j s_{ij}$, loses its correlation only after $\sim 5\tau_\eta$ whereas for $\frac{1}{2}(\mathrm{D}\boldsymbol{\omega}^2/\mathrm{D}t)$ decorrelation happens quickly in $\sim \tau_\eta$. An interesting question is why $\omega_i\omega_j s_{ij}$ is so little disturbed by the relatively large fluctuations of $\boldsymbol{\omega}^2$. Apparently the interaction of vorticity and strain can buffer such fluctuations. If we recall that the magnitude of $\boldsymbol{\omega}^2$ defines just how strong the alignment of vorticity with $\boldsymbol{\lambda}_2$ is, then this buffering effect becomes very plausible. A stronger $\boldsymbol{\lambda}_2$-alignment shifts the main contribution to $\omega_i\omega_j s_{ij}$ from the strong term $\boldsymbol{\omega}^2\Lambda_1\cos^2(\boldsymbol{\omega}, \boldsymbol{\lambda}_1)$ to the weaker term $\boldsymbol{\omega}^2\Lambda_2\cos^2(\boldsymbol{\omega}, \boldsymbol{\lambda}_2)$ and vice versa.

It would be incorrect to infer from the above results that $\nu\omega_i\nabla^2\omega_i$ could be dynamically more important than $\omega_i\omega_j s_{ij}$, since it is $\omega_i\omega_j s_{ij}$ that is producing enstrophy – not much affected by viscous fluctuations – from the constantly smoothed $\boldsymbol{\omega}$ field left by $\nu\omega_i\nabla^2\omega_i$. Taking the view that it is the main role of $\nu\omega_i\nabla^2\omega_i$ to control the overall level of enstrophy by smoothing the field of vorticity, then it seems that $\nu\omega_i\nabla^2\omega_i$ is 'over-reacting' considerably. However, taking into account the above results on the role played by viscosity in $\boldsymbol{\lambda}_2$-alignments and reports of viscous effects that might be related to vortex reconnection and collapse (Kida & Takaoka 1994; Fernandez *et al.* 1995), and thus to fast enstrophy changes, it is not surprising that the behaviour of $\frac{1}{2}(\mathrm{D}\boldsymbol{\omega}^2/\mathrm{D}t)$, which presumably is mainly governed by $\nu\omega_i\nabla^2\omega_i$, is qualitatively different from that of $\omega_i\omega_j s_{ij}$. Viscosity in combination with vorticity is involved in not just one but three areas: balancing overall enstrophy production, adjusting the fine-scale structure of turbulence in order to predominantly align vorticity with the intermediate principal strain axis $\boldsymbol{\lambda}_2$ and possibly continuously altering the topology of turbulent flow by means of vortex reconnection. The large variations we observe for enstrophy changes may then be viewed as the reflection of the sum of these three processes. In any case, it seems clear that the role of the viscous term $\nu\omega_i\nabla^2\omega_i$ plays in enstrophy dynamics is of utmost importance. To gain further insight into the viscous enstrophy mechanisms of production balancing, growth moderating and topology modifications, Lagrangian measurements that can directly access the vector $\nabla^2\omega$ are needed.

5. Concluding remarks

For the first time it has been possible to experimentally measure in a Lagrangian way the full set of velocity derivatives, $\partial u_i/\partial x_j$, along particle trajectories in a turbulent flow. From the results we obtain a picture of vorticity being actively involved in self-regulating processes of production, moderating and reduction via dynamic interaction with its surrounding flow and viscosity.

The critical steps that made it possible to go from three-dimensional particle tracking velocimetry (3D-PTV) measurements of velocities and accelerations to measurements of velocity derivatives are a new 'spatiotemporal' particle tracking algorithm (Willneff 2003), a weighted linear interpolation to obtain velocity derivatives and a weighted polynomial fitting procedure, the beneficial impact of which is demonstrated. The final quality of the velocity derivatives is assessed with checks

based on precise kinematic relations. They show that the technique presented measures the velocity derivatives with good accuracy. The error margin for $\partial u_i/\partial x_j$ is $\sim 14\%$ and for higher-order terms such as enstrophy $\omega_i\omega_j s_{ij}$ it is still only $\sim 30\%$.

Selected Eulerian results on geometrical statistics for vorticity and for strain as well as Lagrangian results on the temporal evolution of infinitesimal material elements prove the capability of 3D-PTV to reproduce most of the relevant results on turbulent fine-scale structure. Most of these features are not observed in a Gaussian flow field, i.e. reflect genuine fluid turbulence. Unlike the non-intrusive measurements presented previously such results were known only from DNS and hot-wire experiments (e.g. Ashurst *et al.* 1987; Kholmyansky *et al.* 2001) for geometrical statistics and from DNS studies (Girimaji & Pope 1990; Dresselhaus & Tabor 1991; Huang 1996) for material elements.

From these results it follows that enstrophy dynamics include processes like self-amplification, $\langle\omega_i\omega_j s_{ij}\rangle > 0$, growth moderation since $\langle\omega_i\omega_j s_{ij}/\omega^2\rangle < \langle l_i l_j s_{ij}/l^2\rangle$ and $\cos(\omega, \lambda_2) \approx 1$ for high $\boldsymbol{\omega}^2$ and s^2, and viscous destruction that balances $\langle\omega_i\omega_j s_{ij}\rangle > 0$. In this paper we focus our attention on the fact that $\cos(\omega, \lambda_2) \approx 1$ is not solely driven and maintained by viscosity but also to a significant degree by vorticity itself. From Lagrangian measurements of special material elements, $\boldsymbol{l}$, which at some moment are identical to vorticity lines, we can confirm that viscosity is an important prerequisite for $\boldsymbol{\lambda}_2$-alignment as was reported by Tsinober & Galanti (2001) and Ohkitani (2002), since without it, $\boldsymbol{\lambda}_1$-alignment is developing, though only slowly. However, the results suggest that there is yet another effect which assists viscosity in keeping vorticity predominantly aligned with $\boldsymbol{\lambda}_2$. We identify an active self-moderating mechanism for enstrophy. We conclude that the deformation tensor, $\boldsymbol{B}$, experiences restricted rotation with respect to vorticity especially for high-enstrophy events, since we find that $\boldsymbol{l}$, which are defined through $\boldsymbol{B}$, keep their initial alignment with $\boldsymbol{\omega}$ up to $6\tau_\eta$. From this we infer that the rotation of the tensor, $\partial u_i/\partial x_j$, is also restricted. As a consequence, the eigenframe, $\boldsymbol{\lambda}_i$, of its symmetric part, s_{ij}, and in particular the orientation of the eigenvector $\boldsymbol{\lambda}_2$ with respect to $\boldsymbol{\omega}$ become much more stable. Thus the alignment of strong vorticity with $\boldsymbol{\lambda}_2$ is much less dependent on the viscous term, $\nu\omega_i\nabla^2\omega_i$. The overall consequence is that enstrophy – especially when it is high – through the interaction of vorticity with its surrounding flow, exhibits a nonlinear saturation, with contributions to $\omega_i\omega_j s_{ij}$ that are associated with the weaker term $\boldsymbol{\omega}^2\Lambda_2\cos^2(\boldsymbol{\omega}, \boldsymbol{\lambda}_2)$ rather than with $\boldsymbol{\omega}^2\Lambda_1\cos^2(\boldsymbol{\omega}, \boldsymbol{\lambda}_1)$.

Investigating the balancing of $\omega_i\omega_j s_{ij}$ through $\nu\omega_i\nabla^2\omega_i$ we looked at the pointwise relation between two of the enstrophy budget terms. Contrary to the observation that the overall enstrophy production and its viscous destruction integrated over the entire domain are approximately balanced at any moment (Tsinober 2001), we found large local $\frac{1}{2}(\mathrm{D}\boldsymbol{\omega}^2/\mathrm{D}t)$ events that can only be driven by equally large $\nu\omega_i\nabla^2\omega_i$ events, since enstrophy production, $\omega_i\omega_j s_{ij}$, is observed to be only weakly correlated with $\frac{1}{2}(\mathrm{D}\boldsymbol{\omega}^2/\mathrm{D}t)$. The balancing of enstrophy production and its viscous destruction is thus concluded to be a non-local process. The observed behaviour is explained in part by the Lagrangian auto-correlations of the enstrophy budget terms. From different correlation coefficients we infer that values of $\frac{1}{2}(\mathrm{D}\boldsymbol{\omega}^2/\mathrm{D}t)$ and thus also of $\nu\omega_i\nabla^2\omega_i$ fluctuate relatively fast, presumably around a slower changing value of $-\omega_i\omega_j s_{ij}$. This results in a balancing in a Lagrangian sense, i.e. averaged over a few time scales along a particle trajectory the level of enstrophy will be stable. The fact that $\omega_i\omega_j s_{ij}$ keeps its correlation over a relatively long time is explained by the $\boldsymbol{\lambda}_2$-alignment with vorticity that is strongly determined by the strength of enstrophy, thus $\boldsymbol{\lambda}_2$-alignment is effectively buffering the strength of $\omega_i\omega_j s_{ij}$.

This completes the picture of vorticity that is actively involved in the control and self-regulation of its evolution, through nonlinear interaction with the strain field and through viscosity. Diffusivity plays an important role in these dynamics, a role that is qualitatively more than just smoothing out the field of vorticity. With respect to vorticity we see that diffusivity is involved in three areas. As reported in Tsinober & Galanti (2001) and Ohkitani (2002) and as demonstrated above, viscosity has a dominant role in $\boldsymbol{\lambda}_2$-alignments. Second, as summarized in Kida & Takaoka (1994), Fernandez *et al.* (1995) and references therein, there are reports of viscous effects that are related to vortex reconnection and collapse, and third, the term $\nu\omega_i\nabla^2\omega_i$ maintains a balance of the growth of vorticity through $\omega_i\omega_j s_{ij}$ in a non-local way. We arrive at the conjecture that the large variations in $\frac{1}{2}(\mathrm{D}\boldsymbol{\omega}^2/\mathrm{D}t)$ – and therefore also in $\nu\omega_i\nabla^2\omega_i$ – reflect the sum of these three involvements. The role the viscous term $\nu\omega_i\nabla^2\omega_i$ plays in enstrophy dynamics is thus of utmost importance. Lagrangian measurements that can directly access the vector $\nabla^2\boldsymbol{\omega}$ are needed and will help to elucidate viscous mechanisms such as balancing overall enstrophy production, adjusting the fine-scale structure of turbulence to predominantly align strong vorticity with $\boldsymbol{\lambda}_2$, and the phenomenon of vortex reconnection which is responsible for continuously altering the topology of turbulent flow.

The above requirement is also stressed by Tsinober & Galanti (2003). They found that the λ_2-alignment of passive vectors with a diffusive term can be observed only for an NSE velocity field, but not for a Gaussian velocity field. In a Gaussian velocity field these vectors align with λ_1, as is observed for artificial (quasi-Gaussian) velocity fields, material lines in NSE numerical experiments and experimentally. Thus, the presence of diffusivity/viscosity is only a necessary but not sufficient ingredient to explain λ_2-alignment of passive vectors with a diffusive term and vorticity. Further study is necessary, which to our view requires looking into Lagrangian aspects of the problem as mentioned above.

Appendix A. Low-pass filtering of particle positions

Determining velocities, u_i, and accelerations, a_i, through central differences is only first-order accurate and hence very sensitive to particle position errors, which in our experiment are of $O(10\,\mu\mathrm{m})$. Therefore the entire position signal, $x_i(t)$, of each trajectory is low-pass filtered with a cut-off frequency of 10 Hz and filtered velocity and acceleration signals, $\widehat{u_i}(t)$ and $\widehat{a_i}(t)$, are derived as first and second derivatives from $\widehat{x_i}(t)$. The frequency of 10 Hz is chosen in order to be well above the maximal position signal frequency of 5 Hz, which can be estimated from $\tau_\eta = 0.26\,\mathrm{s}$, and well below 30 Hz, which with a 60 Hz recording rate is the highest resolvable frequency. The filter is implemented as a moving cubic spline of type

$$\widehat{x_i}(t) = c_{i,o} + c_{i,1}t + c_{i,2}t^2 + c_{i,3}t^3. \tag{A 1}$$

To obtain the desired cut-off frequency the constants $c_{i,j}$ from expression (A 1) are fitted to 21 trajectory points from $t - 10\Delta t$ to $t + 10\Delta t$ for each component, x_1, x_2, x_3, around each time step t. The filtered velocities and accelerations are then defined as the first and second derivatives of expression (A 1) as

$$\widehat{u_i}(t) = c_{i,1} + 2c_{i,2}t + 3c_{i,3}t^2 \tag{A 2}$$

and

$$\widehat{a_i}(t) = 2c_{i,2} + 6c_{i,3}t. \tag{A 3}$$

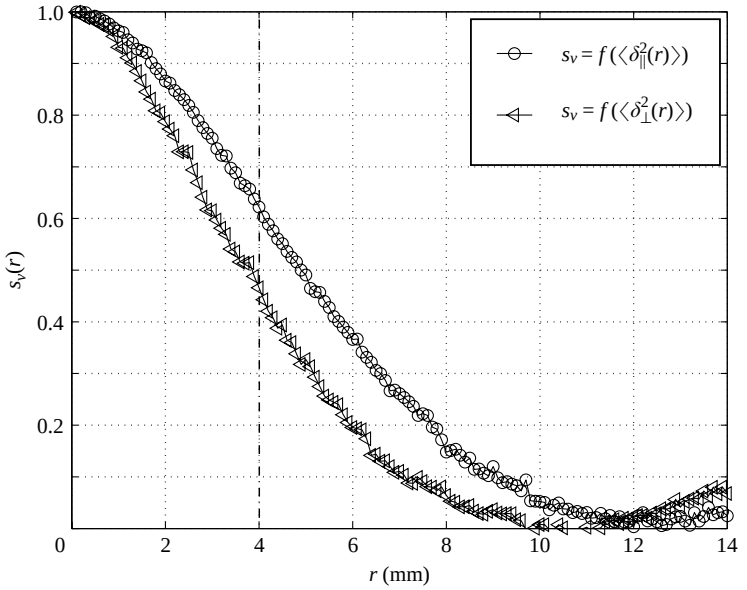

FIGURE 14. The validity of the ansatz that the velocity field is linear in the proximity of x at a distance r is estimated with expression (B 3).

Appendix B. Upper bound for viscous subrange

An upper bound for the viscous subrange separations, s_v, is estimated indirectly through the longitudinal second-order structure function

$$\left\langle \delta v_\parallel^2(r) \right\rangle = C_K(\varepsilon r)^{2/3}, \tag{B 1}$$

which is valid for inertial subrange separations. If expression (B 1) is rearranged for ε as

$$g(r) = \left(\frac{\left\langle \delta v_\parallel^2(r) \right\rangle}{C_K} \right)^{3/2} \frac{1}{r}, \tag{B 2}$$

$g(r)$ reaches a plateau in the inertial range at $g_{\max} \sim \varepsilon$. An estimate of how far r is still within the viscous subrange, or how far the linear ansatz is still valid, is then given by

$$s_v(r) = \frac{g_{\max} - g(r)}{g_{\max}}. \tag{B 3}$$

The function $s_v(r)$ as obtained for our experiment is shown in figure 14. Up to $r \approx 4\,\text{mm}$ $s_v(r)$ is larger than 0.5 and it was therefore chosen to include all particles that remain within a sphere of radius 4 mm to solve expression (7).

Appendix C. Weighted fit along particle trajectories

Polynomials of type

$$\frac{\partial u_i}{\partial x_j}(t)\,,\ \frac{\partial u_i}{\partial t}(t) = \sum_{k=0}^{n} c_k\, t^k \tag{C 1}$$

and of adequate order, n, are fitted to each velocity derivative signal, $\partial u_i/\partial(\cdot)$, along the entire trajectory of length, ℓ, where the contribution of every particle trajectory

point is weighted according to the local quality of the linear interpolation. n is chosen high enough to properly resolve the relevant fluctuations but not too high, in order obtain poorly conditioned matrices $\boldsymbol{A}^T\boldsymbol{A}$. Those have to be inverted when solving the overdetermined system of linear equations, $\boldsymbol{A}\boldsymbol{c}=\boldsymbol{d}$ as

$$\boldsymbol{c}_i = (\boldsymbol{A}^T\boldsymbol{d})(\boldsymbol{A}^T\boldsymbol{A})^{-1}, \tag{C 2}$$

where $\boldsymbol{A}$ is a weighted time matrix

$$\boldsymbol{A} = \begin{bmatrix} (1 & t_1^1 & t_1^2 & \dots & t_1^n)w_1 \\ (1 & t_2^1 & t_2^2 & \dots & t_2^n)w_2 \\ \dots & \dots & \dots & \dots & \dots \\ (1 & t_\ell^1 & t_\ell^2 & \dots & t_\ell^n)w_\ell \end{bmatrix} \quad \text{and} \quad \boldsymbol{d} = \begin{bmatrix} \dfrac{\partial u_i}{\partial(\cdot)}(t_1)w_1 \\ \dfrac{\partial u_i}{\partial(\cdot)}(t_2)w_2 \\ \dots \\ \dfrac{\partial u_i}{\partial(\cdot)}(t_\ell)w_\ell \end{bmatrix}.$$

It is found that a good choice for n is 3 when the trajectory length, ℓ, is up to $1.5\tau_\eta$, $n=4$ for $1.5\tau_\eta \leqslant \ell \leqslant 2.5\tau_\eta$, $n=5$ for $2.5\tau_\eta \leqslant \ell \leqslant 3.5\tau_\eta$ and so forth. As a measure for the local interpolation quality we use relative divergence, δ, defined in expression (11). The weights w_i are obtained as

$$w_i = 1-(1+\exp(-10(\delta(t_i)-0.25)))^{-1}. \tag{C 3}$$

With the sigmoidal function of expression (C 3) high-quality δ values close to zero result in $w_i \approx 1$, the still acceptable quality of $\delta \approx 0.2$ results in $w_i \approx 0.6$ and for relative divergences higher than 0.3 the weights decay below 0.2.

Appendix D. Accuracies for higher-order terms

With a completely analogous approach as for the errors of $\partial u_i/\partial x_j$, $\boldsymbol{a}$, $\boldsymbol{a}_l$, $\boldsymbol{a}_c$ and $l_j\partial u_i/\partial x_j$ we can also estimate errors for the higher-order terms $\frac{1}{2}(\mathrm{D}\omega^2/\mathrm{D}t)$, $\omega_i\omega_j s_{ij}$, $\nu\omega_i\nabla^2\omega_i$ and their corresponding terms $\frac{1}{2}(\mathrm{D}l^2/\mathrm{D}t)$ and $l_i l_j s_{ij}$. For the term $\varepsilon_{\frac{1}{2}\mathrm{D}\omega^2/\mathrm{D}t}$ we write

$$\varepsilon_{\frac{1}{2}\mathrm{D}\omega^2/\mathrm{D}t} = 0.7\left[\frac{1}{2}\varepsilon_{\omega^2}\frac{1}{\Delta t}\left(\frac{\ell}{c}\right)^{-1/2}\right], \tag{D 1}$$

where the factor $(\ell/c)^{-1/2x}$ accounts for the fact that $\boldsymbol{\omega}^2$ is essentially fitted to a polynomial with $c=4$ constant along trajectories with length ℓ and the factor 0.7 accounts for the effect of selecting only data with $\delta<0.1$. In our experiment we typically have $\ell \approx 30$. With

$$\begin{aligned}\varepsilon_{\omega^2} &= \left(\omega+\varepsilon_{\partial u/\partial x}\right)\left(\omega+\varepsilon_{\partial u/\partial x}\right)-\omega^2 \\ &\approx 2O(\omega)\varepsilon_{\partial u/\partial x},\end{aligned} \tag{D 2}$$

$\varepsilon_{\partial u/\partial x} \approx 0.14\,\mathrm{s}^{-1}$, $O(\omega)=3\,\mathrm{s}^{-1}$, and rms $(\frac{1}{2}\mathrm{D}\omega^2/\mathrm{D}t)=12\,\mathrm{s}^{-3}$ we find

$$\begin{aligned}\varepsilon_{\frac{1}{2}\mathrm{D}\omega^2/\mathrm{D}t} &\approx 0.7\times\frac{1}{2}\times 2O(\omega)\varepsilon_{\partial u/\partial x}60\,\mathrm{Hz}\left(\frac{30}{4}\right)^{-1/2} \\ &= 4.3\,\mathrm{s}^{-3} = 36\%\text{ of r.m.s.}\end{aligned} \tag{D 3}$$

For $\varepsilon_{\omega\omega s}$ we have

$$\varepsilon_{\omega\omega s} = 0.7\left[\left(\omega+\varepsilon_{\partial u/\partial x}\right)\left(\omega+\varepsilon_{\partial u/\partial x}\right)\left(s+\varepsilon_{\partial u/\partial x}\right)-\omega_i\omega_j s_{ij}\right]. \tag{D 4}$$

With $O(\omega^2) = 8\,\mathrm{s}^{-2}$, $O(s^2) = 4\,\mathrm{s}^{-2}$ and rms $(\omega_i \omega_j s_{ij}) = 6\,\mathrm{s}^{-3}$ we find

$$\begin{aligned} \varepsilon_{\omega\omega s} &\approx O(\omega^2)\varepsilon_{\partial u/\partial x} + 2O(\omega)O(s)\varepsilon_{\partial u/\partial x} \\ &= 1.9\,\mathrm{s}^{-3} = 32\,\% \text{ of r.m.s.} \end{aligned} \tag{D 5}$$

The error of the viscous term, $\nu\omega_i\nabla^2\omega_i$, which at present can be obtained only as the difference of $\frac{1}{2}(\mathrm{D}\omega^2/\mathrm{D}t)$ and $\omega_i\omega_j s_{ij}$ is then estimated as

$$\varepsilon_{\nu\omega\nabla^2\omega} = \frac{\varepsilon_{\frac{1}{2}\mathrm{D}\omega^2/\mathrm{D}t} + \varepsilon_{\omega\omega s}}{\sqrt{2}} \approx 48\% \text{ of r.m.s.}$$

The errors for the related quantities $\frac{1}{2}(\mathrm{D}l^2/\mathrm{D}t)$ and $l_i l_j s_{ij}$, $\varepsilon_{\mathrm{D}l^2/\mathrm{D}t}$ and ε_{lls} are derived in a completely analogous fashion and are

$$\begin{aligned} \varepsilon_{\mathrm{D}l^2/\mathrm{D}t} &\approx 0.7\left[\frac{1}{2}2O(l)\varepsilon_{\tilde{l}}60\,\mathrm{Hz}\left(\frac{30}{4}\right)^{-1/2}\right] \\ &= 0.9\,\mathrm{mm}^2\,\mathrm{s}^{-1} = 13\% \text{ of r.m.s.}, \end{aligned} \tag{D 6}$$

with $O(l) = 3.5\,\mathrm{mm}$ and $\varepsilon_l = 0.02\,\mathrm{mm}$;

$$\begin{aligned} \varepsilon_{lls} &\approx 0.7\left[O(l^2)\varepsilon_{\partial u/\partial x} + 2O(l)O(s)\varepsilon_{\partial u/\partial x}\right] \\ &= 2.6\,\mathrm{mm}^2\,\mathrm{s}^{-1} = 37\% \text{ of r.m.s.}, \end{aligned} \tag{D 7}$$

with $O(l^2) = 12.25\,\mathrm{mm}^2$.

REFERENCES

Ashurst, W. T., Kerstein, A. R., Kerr, R. A. & Gibson, C. H. 1987 Alignment of vorticity and scalar gradient with strain rate in simulated Navier-Stokes turbulence. *Phys. Fluids* **30**, 2343–2353.

Batchelor, G. K. 1952 The effect of homogeneous turbulence on material lines and surfaces. *Proc. R. Soc. Lond.* A **213**, 349.

Batchelor, G. K. & Townsend, A. A. 1949 The nature of turbulent motion at large wave-numbers. *Proc. R. Soc. Lond.* A **199**, 238–255.

Betchov, R. 1956 An inequality concerning the production of vorticity in isotropic turbulence. *J. Fluid Mech.* **1**, 497–503.

Brachet, M. E., Meneguzzi, M., Vincent, A. Politano, H. & Sulem, P. L. 1992 Numerical evidence of smooth self-similar dynamics and possibility of subsequent collapse for three-dimensional ideal flows. *Phys. Fluids* A **4**, 2845–2854.

Cantwell, B. J. 1992 Exact solution of a restricted Euler equation for the velocity gradient tensor. *Phys. Fluids* A **4**, 782–793.

Cardoso, O., Glukmann, B., Parcolet, O. & Tabeling, P. 1996 Dispersion in a quasi-two-dimensional-turbulent flow: An experimental study. *Phys. Fluids* **8**, 209–214.

Chacin, J., Cantwell, B. J. & Kline, S. J. 1996 Study of turbulent boundary layer using invariants of the velocity gradient tensor. *Expl. Thermal Fluid Sci.* **33**, 308–317.

Chang, T. & Taterson, G. 1983 Application of image processing to the analysis of three-dimensional flow fields. *Opt. Engng* **23**, 283–287.

Chertkov, M., Pumir, A. & Shraiman, B. I. 1999 Lagrangian tetrahedron dynamics and the phenomenology of turbulence. *Phys. Fluids* **11**, 2394–2410.

Constantin, P. 1994 Geometrical statistics in turbulence. *SIAM Rev.* **36**, 73–98.

Dresselhaus, E. & Tabor, M. 1994 The kinematics of stretching and alignment of material elements in general flow fields. *J. Fluid Mech.* **236**, 415–444.

Fernandez, V. M., Zabusky, N. J. & Gryanik, V. M. 1995 Vortex intensification and collapse of the Lissajous-elliptic ring: single- and multi-filament Biot-Savart simulations and visiometrics. *J. Fluid Mech.* **299**, 289–331.

Galanti, B. & Tsinober, A. 2000 Self-amplification of the field of velocity derivatives in quasi-isotropic turbulence. *Phys. Fluids* **12**, 3097–3099; erratum *Phys. Fluids* **13**, 1063 (2001).

Galanti, B. & Tsinober, A. 2004 Comparative study of vorticity and passive vectors in numerical turbulence. *Fluid Dyn. Res.* (submitted).

Girimaji, S. S. & Pope, S. B. 1990 Material-element deformation in isotropic turbulence. *J. Fluid Mech.* **220**, 427–458.

Honji, H., Ohkura, M. & Ikehata, Y. 1997 Flow patterns of an array of electro-magnetically-driven cellular vortices. *Exps. Fluids* **23**, 141–144.

Huang, M.-J. 1996 Correlations of vorticity and material line elements with strain in decaying turbulence. *Phys. Fluids* **8**, 2203.

Hunt, J. C. R. 1973 Review of Tennekes, H. and Lumley, J. L. "*A First Course in Turbulence*". *J. Fluid Mech.* **58**, 817.

Kholmyansky, M. Tsinober, A. & Yorish, S. 2001 Velocity derivatives in the atmospheric turbulent flow at $Re_\lambda = 10^4$. *Phys. Fluids* **13**, 311–314.

Kida, S. & Takaoka, M. 1994 Vortex reconnection. *Annu. Rev. Fluid Mech.* **26**, 169–189.

Kolmogorov, A. N. 1941*a* The local structure of turbulence in incompressible viscous fluid for very large Reynolds numbers. *Dokl. Akad. Nauk SSSR*, **30**, 299–303; English translation *Selected Works of A. N. Kolmogorov*, vol. I (ed. V. M. Tikhomirov), pp. 321–318, Kluwer, 1991.

Kolmogorov, A. N. 1941*b* Dissipation of energy in locally isotropic turbulence, *Dokl. Akad. Nauk SSSR*, **32**, 19–21; English translation *Selected Works of A. N. Kolmogorov*, vol. I (ed. V. M. Tikhomirov), pp. 324–327, Kluwer, 1991.

La Porta, A., Voth, G. A., Crawford, A. M., Alexander, J. & Bodenschatz, E. 2001 Fluid particle accelerations in fully developed turbulence. *Nature* **409**, 1017–1019.

Lüthi, B. 2002 Some aspects of strain, vorticity and material element dynamics as measured with 3D particle tracking velocimetry. ETH Zürich, PhD Thesis.

Lüthi, B., Burr, U., Kinzelbach, W. & Tsinober, A. 2001 Velocity derivatives in turbulent flow from 3D-PTV measurements. In *Proc. Second Intl Symp. on Turbulence and Shear Flow Phenomena, Stockholm, 27–29 June 2001*, vol. II (ed. E. Lindborg *et al.*), pp. 123–128.

Maas, H.-G. 1992 Digitale Photogrammetrie in der dreidimensionalen Strömungs-messtechnik. ETH Zürich, PhD Thesis.

Maas, H.-G., Grün, A. & Papantoniou, D. 1993 Particle tracking velocimetry in three-dimensional flows, Part I. Photogrammetric determination of particle coordinates. *Exps. Fluids* **15**, 133–146.

Malik, N. Dracos, T. & Papantoniou, D. 1993 Particle tracking velocimetry in three-dimensional flows, Part II. Particle Tracking. *Exps. Fluids* **15**, 279–294.

Mann, J., Ott, S. & Andersen, J. S. 1999 Experimental study of relative, turbulent diffusion. *RISOE-R-1036(EN)*, RISOE Natl Lab., Roskilde, Denmark.

Monin, A. S. & Yaglom, A. M. 1997 *Statistical Fluid Mechanics, The Mechanics of Turbulence*, New English edition vol. 1, Chapters 2 and 3. CTR Monographs, NASA Ames – Stanford University.

Novikov, E. A. 1967 Kinetic equations for a vortex field. *Dokl. Akad. Nauk SSSR*, **177**(2), 299–301; English translation *Sov. Phys. Dokl.* **12**(11), 1006–1008 (1968).

Obukhov, A. M. 1983 Kolmogorov flow and laboratory simulation of it. *Russian Math. Surveys* **38**(4), 113–126.

Ohkitani, K. 2002 Numerical study of comparison of vorticity and passive vectors in turbulence and inviscid flows. *Phys. Rev.* E **65**, 046304, 1–12.

Ohkitani, K. & Kishiba, S. 1995 Nonlocal nature of vortex stretching in an inviscid fluid. *Phys. Fluids* **7**, 411–421.

Ooi, A., Martin, J., Soria, J. & Chong, M. S. 1999 A study of the evolution and characteristics of invariants of the velocity-gradient tensor in isotropic turbulence. *J. Fluid Mech.* **381**, 141–174.

Ott, S. & Mann, J. 2000 An experimental investigation of the relative diffusion of particle pairs in three-dimensional turbulent flow. *J. Fluid Mech.* **422**, 207–223.

Perry, A. E. & Fairlie, B. D. 1974 Critical points in flow patterns. *Adv. Geophys.* **18** B, 299–315.

Proudman, I. & Reid, W. H. 1954 On the decay of a normally distributed and homogeneous turbulent velocity field. *Phil. Trans. R. Soc. Lond.* A **247**, 163–189.

Pumir, A., Shraiman, B. I. & Chertkov, M. 2000 Geometry of Lagrangian dispersion in turbulence. *Phys. Rev. Lett.* **85**(25), 5324–5327.

Racca, R. & Dewey, J. 1988 A method for automatic particle tracking in a three-dimensional flow field. *Exps. Fluids* **6**, 25–32.

Sato, Y. & Yamamoto, K. 1987 Lagrangian measurement of fluid-particle motion in an isotropic turbulent field. *J. Fluid Mech.* **175**, 183–199.

Shtilman, L., Spector, M. & Tsinober, A. 1993 On some kinematic versus dynamic properties of homogeneous turbulence. *J. Fluid Mech.* **247**, 65–77.

Siggia, E. D. 1981 Numerical study of small-scale intermittency in three-dimensional turbulence. *J. Fluid Mech.* **107**, 375–406.

Snyder, W. H. & Lumley, J. L. 1971 Some measurements of particle velocity autocorelation functions in a turbulent motion. *J. Fluid Mech.* **48**, 41–71.

Stüer, H. 1999 Investigation of separation on a forward facing step. PhD thesis, ETH-Zürich.

Taylor, G. I. 1937 The statistical theory of isotropic turbulence. *J. Aeronaut. Sci.* **4**, 311–315.

Taylor, G. I. 1938 Production and dissipation of vorticity in a turbulent fluid. *Proc. R. Soc. Lond.* A **164**, 15–23.

Tennekes, H. & Lumley, J. L. 1972 *A First Course in Turbulence*. MIT Press.

Tsinober, A. 2000 Vortex stretching versus production of strain/dissipation. In *Turbulence Structure and Vortex Dynamics* (ed. J. C. R. Hunt & J. Vassilicos), pp. 164–191. Cambridge University Press.

Tsinober, A. 2001 *An Informal Introduction to Turbulence*. Kluwer.

Tsinober, A. & Galanti, B. 2001 Numerical experiments on geometrical statistics of passive objects in turbulent flows. *EUROMECH Workshop 428 26–29 September, Transport by Coherent Structures in Environmental and Geophysical Flows, Torino.*

Tsinober, A. & Galanti, B. 2003 Exploratory numerical experiments on the differences between genuine and 'passive' turbulence. *Phys. Fluids* **15**, 3514–3531.

Tsinober, A. Kit, E. & Dracos, T. 1992 Experimental investigation of the field of velocity gradients in turbulent flows. *J. Fluid Mech.* **242**, 169–192.

Tsinober, A., Shtilman, L. & Vaisburd, H. 1997 A study of vortex stretching and enstrophy generation in numerical and laboratory turbulence. *Fluid Dyn. Res.* **21**, 477–494.

Vincent, A. & Meneguzzi, M. 1994 The dynamics of vorticity tubes in homogeneous turbulence. *J. Fluid Mech.* **258**, 245–254.

Virant, M. 1996 Anwendung des dreidimensionalen "Particle-Tracking-Velocimetry" auf die Untersuchung von Dispersionsvorgängen in Kanalströmungen. ETH Zürich, Ph.D. Thesis.

Virant, M. & Dracos, T. 1997 3D PTV and its application on Lagrangian motion. *Meas. Sci. Tech.* **8**, 1539–1552.

Voth, G., Satyanarayan, K. & Bodenschatz, E. 1998 Lagrangian acceleration measurements at large Reynold numbers. *Phys. Fluids* **10**, 2268–2280.

Voth, G. A., Haller, G. & Gollub, J. P. 2002 Experimental measurements of stretching fields in fluid mixing. *Phys. Rev. Lett.* **88**(25), 254501, 1–4.

Willneff, J. 2003 A spatio-temporal matching algorithm for 3D-particle tracking velocimetry. ETH Zürich, PhD Thesis.

Yanitskii, V. E. 1982 Transport equation for the deformation-rate tensor and description of an ideal incompressible fluid by a system of equations of the dynamical type. *Sov. Phys. Dokl.* **27**, 701–703.

Yeung, P.-K. 2002 Lagrangian investigation of turbulence. *Annu. Rev. Fluid Mech.* **34**, 115–142.

Yule, A. J. 1975 Turbulent and laminar pipe flow distorted by magnetic forces. *J. Fluid Mech.* **72**, 481–498.